

30th May 2020

Dear Pippa Whitehouse,

RE: Response to Editor Comments

Thank you for your positive comments and suggested changes to the manuscript. We have responded to your comments (please see **red text** below) and have edited our manuscript as appropriate. Please also find attached a revised manuscript with tracked changes. The line numbers we refer to below are taken from the tracked changes manuscript.

Thank you for taking your time to consider our revised manuscript, we hope it is now acceptable for publication.

Kind Regards,

Rebecca Dell and co-authors.

Editor comments

I would like to thank the authors for robustly addressing all of the reviewers' comments.

In the revised manuscript you have carried out a number of revisions that have improved the quality and presentation of the article and I am happy that there are no further major issues to be addressed. I list below a number of very minor technical points. Once these are addressed, I would be happy to accept this article for publication.

Kind regards,

Pippa Whitehouse

Line 47-48: hyphen needed in 'sea-level rise'

Corrected (L47-48)

Line 88: there is an extra space after 'streams'

Corrected (L88)

Line 120: "We develop the FASTER algorithm..." rephrase to indicate that you adapt/update the FASTER algorithm

Corrected to 'adapt' (L122)

Line 129: needs another closing bracket

Corrected (L131)

Line 148: word missing?

Corrected - Inserted 'was' (L151)

Line 162: upon -> on

Corrected (L165)

Line 222: I see you've converted numbers less than 10 into text, but here I think values are best expressed as '0 to 1' (but check the guidelines)

Corrected (L226)

Line 228: S2 -> Sentinel-2

Corrected (L232)

Line 291-292: clarify that you are still talking about Landsat 8 here

Changed 'In our study' to 'For Landsat 8 images' (L297)

Line 312: odd phrasing "pixel with an ice cover" (and at the start of the sentence)

We have reworded this sentence to: 'Pixels in the lake masks that were filled (normally those with a floating ice cover, see section 3.2) were assigned the mean water depth of their respective water bodies.' (L317-319)

Line 383: is -> are

Corrected (L395)

Line 387: listing the period covered by the model is confusing because later in the sentence you state that the model is used to provide a continuous time series from November 2016 to April 2017 – perhaps delete "for the period 20151231T1200Z to 20171230T0000Z" or split the sentence in two, making it clear that you are extracting data from a longer run.

We have split the sentence into two (L398-401).

Line 392: why not extract data from the grid point immediately to the north of Schirmacheroasen, since this is where the lakes are?

Sorry, this is a typo, we did actually use the cell to the north! We have corrected this. (L403)

Line 466: it does not make sense to say that the volume increases at a greater rate than the area because these quantities have different units (similarly line 469).

We have changed this section to: 'Between 17th December 2016 and 27th December 2016 'all water bodies' are effectively deepening, as their mean depth increases whilst the total area increases,

whereas between the 27th December and the 26th January 'all water bodies' are effectively spreading, as their mean depth decreases whilst total area increases. (Table 1, Fig. 7).' (L479-483).

Line 490: figure 9b suggests the elevation of the ES decreases by ~7 m over 27 km

Corrected (L517)

Line 556: perhaps mark the downstream extent of the WS and ES at various dates on figure 9, and include a reference to this figure in the text

Corrected (Fig 9 and L585).

Line 570: clarify that you are talking about figure 11b when you mention 'dark areas'

Corrected (L599).

Line 570: there is an unexplained reference to 'tributary glaciers' on this line

We have removed this and changed the sentence to 'Areas of low backscatter (appearing as dark areas in Figure 11b) extend across the grounding line onto the upper part of the ice shelf.' (L597-600).

Line 572: where relevant, clarify what aspect of these factors would result in low backscatter, e.g. particularly large/small/variable snow-grain size?

We have clarified and included a new reference (Sun et al., 2015) (L600-602):

Whilst areas of low backscatter may result from relatively small dry-snow grain sizes, shallow dry-snow depths to underlying rougher surfaces, high surface roughnesses, or complex internal stratigraphies (Rott and Mätzler, 1987; Sun et al., 2015).

Sun, S., Che, T., Wang, J., Li, H., Hao, X., Wang, Z. and Wang, J.: Estimation and analysis of snow water equivalents based on C-band SAR data and field measurements, Arctic, Antarct. Alp. Res., 47(2), 313–326, doi:10.1657/AAAR00C-13-135, 2015.

Line 577: there is no scale bar to allow the reader to identify the backscatter values

Corrected (Fig.11)

Line 602: topography -> ice shelf surface topography

Corrected (L631)

Line 604: do you know this, and can you make any comment about what happens to the water in the WS and ES at the end of the 2016-17 melt season?

We don't know for certain, but we think it is likely based on the work of Kingslake et al. (2015). We have added 'likely' into our sentence (L633): 'This large scale lateral transfer of meltwater is likely further facilitated as the ES and WS develop over frozen meltwater paths from previous years

(Kingslake et al., 2015). Without further data and analysis we cannot speculate further on what happens to the water at the end of the melt season.

Line 653: hyphen needed in 'meltwater-driven instabilities' ?

Corrected (L687)

Some text is green! Or blue.

Corrected throughout.

Fig. 1: I suggest labelling the ice shelf (or say that the orange shape roughly delineates the ice shelf).

We have adjusted the figure caption as follows: The solid orange line roughly delineates the ice shelf and shows the study area extent used for this study (L1032-2033)

Fig. 2: why are there dot-dash lines around some boxes? May need a little re-designing around the 'Average Water Body Depths' box because this step is not carried out for Sentinel-2 data.

The dot-dash lines indicate steps that were only applied to Landsat 8 images, this is explained in the caption (L1044-1046):

'Dashed lines indicate steps that were applied to Landsat 8 images only, whereas solid lines indicate steps that were applied to both sets of image types.'

Fig. 4: could refer to this figure in section 3.5, i.e. where you first mention the maximum extent mask.

Corrected (L345).

Fig. 5: mention the date stamp in the caption; scale bar text is very small.

We have added the following to the caption: 'Date stamps are in the bottom right hand corner of each image.' We have also increased the font size for the scale bar. (L1070).

Fig. 5 caption (line 1020): there is reference to 'lake and stream' masks rather than circular and linear features

Corrected (L1069).

Fig. 10 caption (line 1058): space missing after 'Schirmacheroasen'

Corrected (L1109).

Fig. 10: 'total volume lost' is plotted as a volume on a specific date, but presumably the meltwater disappears sometime between the previous image and that date? This could be clearer in the caption. Also, if this is correct, then should the volume be scaled to reflect the time period over which the meltwater disappeared?

The 'total volume lost' plot is plotted on the end date by which the circular water body has lost > 80 % of its volume (we call this a loss event). The loss event could have started at any date before this,

not necessarily just at the previous time point. We have therefore not scaled the data to reflect this as we believe the plot would be too busy, and harder to interpret. It is simpler to convey that 'by X date, Y number of lakes have lost > 80 % of their volume, equating to Z m³ of water'. We have edited the caption to better explain the data:

b) The total volume lost in 'loss events' **by each image date** from water bodies in the 'always circular' category (blue bars) and the total combined water volume (blue line). A loss event is defined as a > 80 % loss in water body volume through either lake drainage or freeze-through. The total number of loss events for each date is indicated above each bar. (L1109-1113).

Table 2: terminology refers to 'lakes' and 'streams' rather than linear and circular water bodies

Corrected

I note a couple of very recent papers that are relevant to this study. One is just published, and one has just come online in The Cryosphere Discussions (and I'm not sure whether you would be allowed to cite it, but I thought it worth mentioning). Entirely up to you as to whether you feel it would be useful to include them:

Arthur, J.F., Stokes, C.R., Jamieson, S.S.R., Carr, J.R. & Leeson, A.A. (2020). Recent understanding of Antarctic supraglacial lakes using satellite remote sensing. *Progress in Physical Geography*

Included (L80)

Fair, Z., Flanner, M., Brunt, K. M., Fricker, H. A., and Gardner, A. S.: Using ICESat-2 and Operation IceBridge altimetry for supraglacial lake depth retrievals, *The Cryosphere Discuss.*, <https://doi.org/10.5194/tc-2020-136>, in review, 2020.

Included (Line 712-713). Also added an additional reference here too:

Buzzard, S., Feltham, D. and Flocco, D.: Modelling the fate of surface melt on the Larsen C Ice Shelf, *Cryosphere*, 12(11), 3565–3575, doi:10.5194/tc-12-3565-2018, 2018.

Lateral meltwater transfer across an Antarctic ice shelf

Rebecca Dell^{1,2}, Neil Arnold¹, Ian Willis¹, Alison Banwell^{3,1}, Andrew Williamson¹,
Hamish Pritchard², and Andrew Orr²

¹Scott Polar Research Institute, Lensfield Road, Cambridge, CB2 1ER, UK

²British Antarctic Survey, High Cross, Madingley Road, Cambridge, CB3 0ET, UK

³Cooperative Institute for Research in Environmental Sciences, University of Colorado
Boulder, Boulder, CO, 80309, USA

copernicus-publications

Correspondence to: Rebecca Dell (rld46@cam.ac.uk)

Abstract

Surface meltwater on ice shelves can exist as slush, it can pond in lakes or crevasses, or it can flow in surface streams and rivers. The collapse of the Larsen B Ice Shelf in 2002 has been attributed to the sudden drainage of ~3000 surface lakes, and has highlighted the potential for surface water to cause ice-shelf instability. Surface meltwater systems have been identified across numerous Antarctic ice shelves, although the extent to which these systems impact ice-shelf instability is poorly constrained. To better understand the role of surface meltwater systems on ice shelves, it is important to track their seasonal development, monitoring the fluctuations in surface water volume and the transfer of water across ice-shelf surfaces. Here, we use Landsat 8 and Sentinel-2 imagery to track surface meltwater across the Nivlisen Ice Shelf in the 2016-2017 melt season. We develop the Fully Automated Supraglacial-Water Tracking algorithm for Ice Shelves (FASTISh) and use it to identify and track the development of 1598 water bodies, which we classify as either circular or linear. The total volume of surface meltwater peaks on 26th January 2017 at 5.5×10^7 m³. At this time, 63% of the total volume is held within two linear surface meltwater systems, which are up to 27 km long, are orientated along the ice shelf's north-south axis, and follow the surface slope. Over the course of the melt season, they appear to migrate away from the grounding line, while growing in size and enveloping smaller water bodies. This suggests there is large-scale lateral water transfer through the surface meltwater system and the firn pack towards the ice-shelf front during the summer.

1 Introduction

The total mass loss from Antarctica has increased from 40 ± 9 Gt/y in 1979–1990 to 252 ± 26 Gt/y in 2009–2017, providing a cumulative contribution to sea-level rise of 14.0 ± 2.0 mm since 1979 (Rignot et al., 2019). Mass loss from Antarctica will likely increase in the near future due, at least in part, to the shrinkage and thinning of some of its ice shelves (Kuipers Munneke et al., 2014; DeConto and Pollard, 2016; Siegert et al., 2019) and the associated acceleration of inland ice across the grounding lines (Fürst et al., 2016; Gudmundsson et al., 2019). Seven out of 12 ice-shelves that bordered the Antarctic Peninsula have collapsed in the last 50 years (Cook and Vaughan, 2010). One of the most notable events was the

45 February-March 2002 collapse of Larsen B, leading to both an instantaneous and a longer
46 term speedup of the glaciers previously buttressed by the ice shelf (Scambos et al., 2004;
47 Wuite et al., 2015; De Rydt et al., 2015), and resulting in their increased contribution to sea-
48 level rise (Rignot et al., 2004).

49
50 The unforeseen catastrophic disintegration of Larsen B highlighted the unpredictable nature
51 of ice-shelf collapse, and prompted a search for the causes of ice-shelf instability. Current
52 understanding of the factors causing ice-shelf instability stems from the very limited number
53 of airborne and satellite observations prior to and following collapse events (e.g. Glasser
54 and Scambos, 2008; Scambos et al. 2009; Banwell et al., 2014, Leeson et al., 2020),
55 numerical modelling (e.g. Vieli et al. 2006, Banwell et al. 2013, Banwell and MacAyeal,
56 2015), and the few in-situ measurements investigating recent and current ice-shelf
57 processes (e.g. Hubbard et al. 2016; Bevan et al., 2017; Banwell et al. 2019). It has been
58 suggested that the chain reaction drainage of ~3000 surface meltwater lakes, which covered
59 5.3% of the total ice-shelf area and had a mean depth of 0.82 m (Banwell et al., 2014), may
60 have triggered the near-instantaneous break-up of Larsen B (Banwell et al., 2013; Robel
61 and Banwell, 2019), highlighting the potential importance of surface hydrology for ice-shelf
62 instability. The formation of these ~3000 surface lakes has been attributed to the saturation
63 of the ice shelf's firn layer, making it impermeable (Kupiers Munneke et al., 2014; Leeson et
64 al., 2020). Given this possible role of surface water on ice-shelf stability, it is important to
65 monitor changes in the area and volume of surface meltwater systems across ice shelves,
66 and compare any trends with those observed at Larsen B prior to its collapse.

67
68 Kingslake et al. (2017) identified numerous pervasive surface meltwater systems across
69 many of Antarctica's ice shelves. Meltwater production is often highest around grounding
70 lines, driven by high net shortwave radiation associated with low albedo blue ice areas, high
71 net longwave radiation around nunataks, and high sensible heat transfer from adiabatic
72 warming of katabatic (Lenaerts et al., 2017) and foehn winds (Bell et al., 2018; Datta et al.,
73 2019). Ice-shelf hydrological systems may then take several forms as meltwater may: (i)
74 form surface streams and flow downslope (e.g. Liston and Winther, 2005; Bell et al. 2017);
75 (ii) collect in surface lakes (e.g. Langley et al. 2016); (iii) percolate into the sub-surface and
76 refreeze (Luckman et al., 2014; Hubbard et al., 2016; Bevan et al., 2017); (iv) percolate into
77 the subsurface and flow laterally (Winther et al., 1996; Liston et al., 1999); or (v) percolate
78 into the subsurface and form sub-surface lakes and reservoirs (e.g. Lenaerts et al. 2017).
79 Despite the identification of pervasive meltwater systems, very little is known about their
80 spatial and temporal evolution, both between and within melt seasons (Arthur et al., 2020).
81 Furthermore, while surface water ponding and the formation of lakes have been implicated
82 in past ice-shelf collapse (Scambos et al., 2003; Banwell et al., 2013), the formation of
83 surface water streams that route water quickly to the ice-shelf front may not necessarily
84 cause instability but rather mitigate against potential surface meltwater-driven collapse (Bell
85 et al., 2017; Banwell, 2017). Thus, whether future projected increased surface melt on ice
86 shelves forms lakes or flows rapidly to the ocean via streams has important implications for
87 future ice-shelf stability and potential collapse. To better understand the behaviour of
88 surface meltwater lakes and streams, it is important to investigate their spatial and temporal

Deleted:

90 evolution across entire ice shelves through entire summer melt seasons and over multiple
91 melt seasons.

92
93 In this paper, our objective is to develop a tool that can identify surface meltwater bodies on
94 Antarctic ice shelves and track their evolution over time. We build on the work of Pope et al.
95 (2016) and Selmes et al. (2011, 2013) and especially Williamson et al. (2017; 2018a), who
96 developed and used the FAST algorithm for tracking lakes on the Greenland Ice Sheet
97 (GrIS) using MODIS imagery. More specifically, we have adapted the FASTER algorithm of
98 Williamson, et al. (2018b) and Miles et al. (2017), who adapted the FAST method to track
99 GrIS lakes from the higher resolution Landsat 8 and Sentinel-1 and -2 imagery.

100
101 These previous methods need adapting for application on Antarctic ice shelves for three
102 main reasons. First, to account for the observed differences in the geometry of surface
103 meltwater bodies compared to those on the GrIS. Second, to recognise the marked
104 geometry changes that occur over time on Antarctic ice shelves, including the joining of
105 water bodies and the enveloping of some water bodies by others. Third, to identify the
106 apparent transfer of surface melt water over large distances across ice shelves. In
107 Greenland, the majority of surface water bodies form in surface depressions that result from
108 undulations in the bedrock topography and ice flow (Echelmeyer et al., 1991; Sergienko,
109 2013), and therefore these water bodies evolve in the same location on an inter- and intra-
110 annual basis (Banwell et al., 2014; Bell et al., 2018). By contrast, the location of surface
111 water bodies on Antarctic ice shelves reflects variations in the surface topography, which
112 are controlled by a combination of factors including (i) basal channels formed by ocean
113 melting (Dow et al., 2018), (ii) basal crevassing (McGrath et al., 2012), (iii) the development
114 of ice flow-stripes in the grounding zone (Glasser and Gudmundsson, 2012), and (iv) suture
115 zone depressions (Bell et al., 2017). In Antarctica, these factors result in a wide range of
116 surface water body geometries; from circular forms, to long linear features that can traverse
117 significant distances across an ice shelf, and might therefore have significant implications
118 for the lateral transfer of surface meltwater.

119
120 Here, we advance the work of Williamson, *et al.* (2018b) and Miles *et al.* (2017) to produce
121 'FASTISH', a Fully Automated Supraglacial Lake and Stream Tracking Algorithm for Ice
122 Shelves. We adapt the FASTER algorithm for use with Landsat 8 and Sentinel-2 data to
123 make it applicable to Antarctic ice shelves. Such adaptations include: (i) assigning
124 approximate depths to pixels with floating ice cover; (ii) acknowledging the geometric
125 variability of surface water bodies across Antarctica and the impact this variability has on
126 the lateral transfer of surface meltwater by categorising water bodies as either circular or
127 linear; (iii) assigning each water body that is tracked over the melt season to one of four
128 categories (always circular, always linear, simple transitions (from circular to linear or vice
129 versa) and envelopment transitions (where water bodies spread and merge with neighboring
130 circular and linear water bodies to form a new water body, or where a water body splits into
131 smaller circular and linear water bodies)) to quantify and illustrate the interaction between
132 individual water bodies as the melt season progresses. We then apply the FASTISH

Deleted: develop

134 algorithm to the Nivlisen Ice Shelf, Antarctica, for the 2016-2017 melt season; the first full
135 melt season to have data coverage over the ice shelf from both Landsat 8 and Sentinel-2.

136

137 **2 Study Area**

138

139 The Nivlisen Ice Shelf (70.3 °S, 11.3°E), is situated in Dronning Maud Land, East Antarctica,
140 between the Vigrid and Lazarev ice shelves (Fig. 1). It has a surface area of 7,600 km², and
141 is ~ 123 km wide by 92 km long. Ice thickness ranges from 150 m at the calving front to ~
142 700 m towards the ice shelf's grounding line in the southeast, and it exhibits flow velocities
143 of around 20 m a⁻¹ to 130 m a⁻¹ (Horwath et al., 2006). To the southeast of the Nivlisen Ice
144 Shelf, there is a blue ice region maintained by katabatic winds, which extends in a south
145 easterly direction for ~ 100 km (Horwath et al., 2006). This blue ice region is characterised
146 by ablation, and adjoins the exposed bedrock nunatak (called Shirmacheroasen), which is
147 positioned where the ice shelf meets the inland ice (Horwath et al., 2006) (Fig.1). Beyond
148 this blue ice region, towards the north, the ice shelf transitions into an accumulation zone as
149 the firn layer thickens (Horwath et al., 2006). In the 2016-2017 melt season, mean daily
150 near-surface temperatures on the Nivlisen Ice Shelf ranged between ~ -25°C and 2°C, and
151 1.6 % of the study area was occupied by a surface water body at least once during this time.

152 The Nivlisen Ice Shelf was selected for this study as: i) pervasive surface meltwater features
153 have previously been identified here in optical satellite imagery, showing evidence of
154 widespread melt ponding in both circular and linear water bodies (Kingslake et al., 2017); ii)
155 these meltwater features have shown significant development over a melt season, as source
156 lakes upstream of the grounding line appeared to drain laterally, rapidly flooding large areas
157 of the ice shelf (Kingslake et al., 2015); and iii) the ice shelf is relatively small, allowing quick
158 and efficient development and application of FASTISh before its use more widely across
159 larger Antarctic ice shelves.

160

161 **3 Methods**

162

163 There are four main components to the FASTISh algorithm: i) delineating water body areas;
164 ii) calculating water body depths and volumes; iii) categorising water bodies as either circular
165 or linear based on their geometries; iv) tracking individual water bodies and measuring their
166 changing dimensions and geometries over time (Fig.2). These will be discussed in sections
167 3.2 to 3.5 respectively, once the pre-processing steps applied to the imagery used have
168 been outlined (section 3.1).

169

170 **3.1 Images and Pre-Processing**

171

172 **3.1.1 Landsat 8**

173

174 12 Landsat 8 scenes with minimal cloud cover, from between 1st November 2016 and 24th
175 March 2017, and each partially covering the ice-shelf extent, were identified and
176 downloaded from the USGS Earth Explorer website (<https://earthexplorer.usgs.gov>) (Fig.
177 S1). Each scene was downloaded as a Tier 2 data product, in the form of raw digital numbers

Formatted: Line spacing: Multiple 1.15 li

Deleted: up

179 (DN). Bands 2 (blue), 3 (green), 4 (red) and 8 (panchromatic) were used for this study (Fig.
180 2). Bands 2, 3, and 4 have a 30 m spatial resolution, and Band 8 has a 15 m spatial
181 resolution. Image scene values were first converted from DN to Top-of-Atmosphere (TOA)
182 reflectance values. Typically, Landsat scenes are converted to TOA reflectance values
183 using a single solar angle over the whole image scene. However, here we correct each pixel
184 for the specific solar illumination angle, based on metadata stored in the .ANG file, and using
185 the 'Solar and View Angle Generation Algorithm' provided by NASA
186 (https://landsat.usgs.gov/sites/default/files/documents/LSDS-1928_L8-OLI-TIRS_Solar-View-Angle-Generation_ADD.pdf).
187 Converting from DN to TOA values on a per-pixel basis
188 is imperative when mosaicking and comparing images obtained at high latitudes, as the
189 solar angle at the time of acquisition can vary significantly across each scene due to the
190 large change in longitude.

191
192 For each Landsat scene, a cloud mask was generated and downloaded from Google Earth
193 Engine (GEE) using the 'Simple Cloud Score Algorithm'
194 (`ee.Algorithms.Landsat.simpleCloudScore`). The simple cloud score algorithm assigns a
195 'cloud score' to every pixel in the image based on the following criteria: (i) brightness in
196 bands 2 (blue), 3 (green), 4 (red); (ii) brightness in just band 2 (blue); (iii) brightness in bands
197 5 (near infrared), 6 (shortwave Infrared 1) and 7 (shortwave infrared 2); and iv) temperature
198 in band 10 (thermal). The algorithm also uses the Normalised Difference Snow Index (NDSI)
199 to distinguish between clouds and snow, which prevents snow from being incorrectly
200 incorporated in the cloud mask. The NDSI was developed by Hall et al. (2001) to distinguish
201 between snow/ice and cumulus clouds and is calculated from the following bands:

$$202 \quad \text{NDSI} = (\text{Blue} - \text{Near Infrared 1}) / (\text{Blue} + \text{Near Infrared 1}) \quad (1)$$

203
204
205 We found the 'simple cloud score algorithm' to be the most effective cloud masking method
206 for Landsat 8 images, as it assesses each pixel using multiple criteria, making it more
207 effective than any single band threshold. Prior to implementing the FASTISh algorithm, each
208 Landsat scene and corresponding cloud mask was clipped to the study area extent in
209 ArcGIS using the batch clip process. Clipping each scene to the same extent is required
210 when comparing images through the FASTISh algorithm, as tracking individual features over
211 time requires images with a consistent spatial reference frame to determine the location of
212 each water body. The 12 scenes formed six pairs (Fig. S1), with two scenes per day each
213 covering part of the ice shelf. Each scene pair was mosaicked using ArcGIS's 'mosaic
214 to new raster' tool to produce six images providing near-complete coverage of the ice shelf
215 for six days of the 2016-2017 melt season (Fig. S1). All images were projected into the 1984
216 Stereographic South Pole co-ordinate system (EPSG: 3031).

217 218 **3.1.2 Sentinel-2**

219
220 20 Sentinel-2A level-1C scenes obtained between 1st November 2016 and 31st March 2017
221 with minimal cloud cover were downloaded from the Copernicus Hub web site
222 (<https://scihub.copernicus.eu>) (Fig. S1). Bands 2 (blue), 3 (green), 4 (red), and 11 (short

Formatted: Font colour: Text 1

223 wave infrared (SWIR)) were used. Bands 2, 3, and 4 have a spatial resolution of 10 m, and
224 band 11 a spatial resolution of 20 m. The Sentinel-2 data for all bands were downloaded as
225 TOA reflectance values, and were divided by the 'quantification value' of 10,000 (from
226 metadata), to convert the numbers into values that lie within the 0 to 1 range (Traganos et
227 al., 2018). We applied this conversion to bands 2, 3 and 4 as these are the bands used to
228 identify water and calculate its depth, and their values need to be comparable to the values
229 provided by Landsat 8. Each downloaded scene was clipped, mosaicked to produce images
230 with full coverage of the ice shelf, and then re-projected to the WGS 1984 Stereographic
231 South Pole co-ordinate system (EPSG: 3031), in line with the Landsat scenes. As the simple
232 cloud score algorithm had not been adapted for application to Sentinel-2 imagery at the time
233 of writing, we computed a cloud mask for each image using a thresholding approach,
234 whereby pixels were categorised as cloudy if the SWIR band value was > 10,000. This
235 threshold was selected through visually assessing the effectiveness of various thresholds
236 against the corresponding RGB scenes. As the resolution of the original SWIR band was 20
237 m, the resultant cloud masks were resampled using nearest neighbor interpolation to 10 m
238 spatial resolution. On two image dates (14th November 2016 and 25th February 2017), this
239 cloud masking approach was not entirely successful as not all clouds were fully masked.
240 Additional individual masks were manually digitised in ArcGIS to ensure all clouds were
241 masked for these images.

242

243 3.2 Delineating Water Body Areas

244

245 Water body areas were determined using the Normalised Difference Water Index for ice
246 (NDWI_{ice}), which has been widely used previously to calculate the distribution of surface
247 meltwater features on the GrIS and on Antarctic ice shelves (e.g. Yang and Smith 2013;
248 Moussavi et al., 2016; Koziol et al. 2017; Macdonald et al. 2018; Williamson et al. 2018b;
249 Banwell et al. 2019). It is calculated from the normalised ratio of the blue and red bands as:

250

$$251 \text{NDWI}_{\text{ice}} = (\text{Blue} - \text{Red}) / (\text{Blue} + \text{Red}) \quad (2)$$

252

253 These bands were used because water has high reflectance values in the blue band, and
254 there is a relatively large contrast between ice and water in the red band (Yang and Smith,
255 2013). Studies typically apply a single NDWI_{ice} threshold to an image in order to classify
256 pixels as either 'wet' or 'dry' (e.g. Fitzpatrick et al., 2014; Moussavi et al. 2016; Miles et al.
257 2017). Across both Greenland and Antarctica, most studies have used a relatively high
258 NDWI_{ice} threshold of 0.25 to map 'deep' water bodies on ice (Yang and Smith 2013, Bell et
259 al. 2017, Williamson et al. 2018b). The same approach was applied to the Nivlisen Ice Shelf
260 in this study in order to facilitate the detection of deep water bodies only. This is important
261 because if too much shallow water and slush is detected, identifying and subsequently
262 tracking individual water bodies over time becomes difficult. Having applied a 0.25 NDWI_{ice}
263 threshold to each image, the resulting water masks were filtered using a two-dimensional 8-
264 connected threshold (i.e. grouping pixels if they were connected by their edges or corners)
265 to identify each individual water body. Water bodies consisting of ≤ 2 pixels (Landsat 8) and
266 ≤ 18 pixels (Sentinel-2), were removed to ensure only water bodies with an area ≥ 1,800 m²

Deleted: zero

Deleted: one

269 were assessed further. To ensure that pixels with floating ice cover were still included in the
270 analysis, we then used the 'imfill' function within MATLAB to classify any 'dry' pixels situated
271 within a water body as water.

272

273 3.3 Water Body Depth Calculations

274

275 Having identified the extent of water bodies, we use a physically-based approach (Sneed
276 and Hamilton, 2007; Arnold et al., 2014; Banwell et al., 2014, 2019; Pope, 2016; Pope et
277 al., 2016; Williamson et al., 2017, 2018b) based on the original work of Philpot (1989), to
278 calculate pixel water depths. Water depth, z , is calculated from:

279

$$280 z = \frac{[\ln(A_d - R_\infty) - \ln(R_{pix} - R_\infty)]}{g} \quad (3)$$

281

282 where R_{pix} is the satellite-measured pixel reflectance, A_d is the lake-bottom albedo, R_∞ is
283 the reflectance value for optically deep (> 40 m) water, and g is the coefficient associated
284 with the losses made during downward and upwards travel in a water column.

285

286 For the Landsat 8 images, pixel water depths were calculated using TOA reflectance data
287 for both the red and panchromatic bands separately, and then averaging these values to
288 give a single final value (Pope *et al.*, 2016; Williamson *et al.*, 2018b). Pope *et al.* (2016)
289 show that this approach gives the smallest mean difference (0.0 +/- 1.6m) between
290 spectrally-derived and DEM-derived lake depths. However, it should be noted that owing
291 to the rapid attenuation of red light by a water column, this algorithm is only able to retrieve
292 depths up to a maximum of ~ 5 m (Pope *et al.*, 2016). Furthermore, this method assumes:
293 (i) no wind and waves at the water body surface (ii) little to no dissolved/suspended
294 material within the water body, (iii) no inelastic scattering, and (iv) the water body substrate
295 is parallel to the surface and homogenous (Sneed and Hamilton, 2011).

296

297 For Landsat 8 images, the panchromatic band was first resampled using bilinear
298 interpolation from 15 m to 30 m spatial resolution to match the resolution of the red band.
299 For the Sentinel-2 images, water body depths were calculated using the TOA reflectance
300 values in the red band only, as there is no equivalent panchromatic band (Williamson *et al.*
301 2018b). To calculate A_d , the mean reflectance value of the second (Landsat) and sixth
302 (Sentinel) rings of pixels outside of each water body was calculated, following a similar
303 approach used by Arnold *et al.* (2014) and Banwell *et al.* (2014). The second or sixth ring of
304 pixels surrounding each lake was used to avoid calculating A_d from slushy areas that border
305 each water body; sixth-pixel rings were used for Sentinel-2 images as these represent the
306 same distance away from the water body as two-pixel rings in Landsat images. In very rare
307 cases, wet pixels within a water body could have a reflectance higher than the calculated A_d
308 value, leading to negative water depths. All such pixels were removed from the area and
309 depth matrix (Fig. 2).

310

Deleted: In our study

β12 Values for R_{∞} were assessed on an image-by-image basis by taking the minimum
313 reflectance value found over optically deep water (the ocean). For images that did not
314 contain optically deep water, the R_{∞} value was set to 0 (Banwell et al., 2019). For Landsat 8
315 imagery we used a g value of 0.7507 for the red band, and 0.3817 for the panchromatic
316 band (Pope *et al.*, 2016), and for Sentinel-2 imagery, we used a value of 0.8304 (Williamson
β17 *et al.*, 2018b). ~~Pixels in the lake masks that were filled (normally those with a floating ice
β18 cover, see section 3.2) were assigned the mean water depth of their respective water
β19 bodies.~~ Individual water body volumes were calculated by multiplying each pixel area by its
320 calculated water depth, and then summing across the water body. To facilitate comparisons
321 between Landsat 8 and Sentinel-2 data, area and depth arrays generated from Landsat 8
322 images were then resampled to 10 m spatial resolution using nearest neighbour
323 interpolation.
324

Formatted: Line spacing: Multiple 1.15 li

Deleted: Pixels that had a floating ice cover and had been filled (see section 3.2) were assigned the mean depth of their respective water bodies, as it is not possible to calculate the depth of a pixel with an ice cover.

β25 3.4 Classifying Water Body Types

β26
β27 Having produced area and depth masks for each date, each identified water body was
328 categorised as either circular or linear based on its solidity (defined as the proportion of
329 pixels of the water body that fall within its convex hull), which was calculated using the
330 'regionprops' function in MATLAB (Banwell et al. 2014). Linear water bodies have a solidity
331 score closer to 0 reflecting the smaller proportion of wet pixels within the convex hull due to
332 likely greater concavity of the edges, whereas more circular water bodies have a solidity
333 score closer to 1 due to the larger proportion of wet pixels within the convex hull due to the
334 more convex shape. Here, water bodies with a solidity score ≥ 0.45 were classified as
335 circular, and water bodies with a solidity score < 0.45 were classified as linear. This threshold
336 was selected by visually assessing the masks generated from thresholds ranging between
337 0.42 and 0.49, in increments of 0.01, and selecting the threshold that appears to best
338 distinguish between more circular and more linear water bodies (Fig. 3).

β40 3.5 Tracking Water Bodies

β41
β42 A 3D matrix of all water bodies was compiled, recording the area and volume of each water
343 body over time, as well as whether the water body had a circular or linear geometry (as
344 defined in section 3.4). To track changes in the area and volume of surface meltwater bodies
β45 throughout the 2016-2017 melt season, a maximum extent mask (Fig. 4b) was also
346 generated by superimposing the areas of all water bodies identified in each image
347 (Williamson *et al.*, 2018b). The maximum extent mask was then used to guide the tracking
348 process. Each individual water body within the maximum extent was prescribed an ID, and
349 changes to the area and volume of each individual water body over time were tracked within
350 its maximum extent (Williamson *et al.*, 2018b).

β51
β52 In addition to tracking changes in the area and volume of each water body, the FASTISH
353 algorithm also tracks the water body type. From this tracking process, four categories were
354 defined: (i) always circular, (ii) always linear, (iii) 'simple transitions' where a water body is
355 defined as *either* circular or linear and switches between the two categories (either once or

361 more than once, and in either direction), and (iv) ‘envelopment transitions’ where water
362 bodies spread and merge with neighbouring circular and linear water bodies to form new,
363 larger bodies, or where larger bodies split into smaller circular and linear water bodies. This
364 final category allows us to track the development of large surface water bodies across the
365 ice-shelf surface as it identifies smaller water bodies being subsumed by larger water bodies
366 as the melt season progresses.

367

368 3.6 Digital Elevation Model

369

370 To aid interpretations of the tracking results produced by the FASTISh algorithm, we used
371 surface elevation data from the Reference Elevation Model of Antarctica (REMA) database
372 (Howat et al., 2019). Figure 4a shows the REMA Digital Elevation Model (DEM) of the ice
373 shelf at 8 m resolution, produced by mosaicking four, 8 m resolution REMA tiles. In
374 addition, a single 2 m REMA data strip from 31st January 2016 was used to extract the
375 elevation profiles along two tracked water bodies, the Eastern System and the Western
376 System, which are introduced in section 4.2.2.

377

378 3.7 Regional climate simulation

379

380 In order to understand how climate variability influences the findings, we analysed results
381 from an atmosphere-only regional climate CORDEX (COordinated Regional climate
382 Downscaling Experiment) simulation of Antarctica using the limited-area configuration of
383 Version 11.1 of the UK Met Office Unified Model (MetUM) for the period 2016-2017. The
384 MetUM is a weather prediction model, which uses a semi-Lagrangian semi-implicit scheme
385 for solving the fully-compressible, non-hydrostatic, deep-atmosphere equations of motion
386 (Walters et al., 2017).

387

388 The setup of the MetUM is similar to that used by Mottram et al. (2020), with the exception
389 that the horizontal resolution for the limited-area Antarctic domain has been increased from
390 50 to 12 km (and consists of 392 × 504 grid points). The Antarctic domain uses the regional
391 atmosphere mid-latitude (RA1M) science configuration (Bush et al., 2019), a rotated
392 latitude-longitude grid in order to ensure that the grid points are evenly spaced, and 70
393 vertical levels up to an altitude of 40 km.

394

395 The required start data and lateral boundary conditions for the Antarctic domain ~~are~~ supplied
396 by a global version run of the MetUM at N320 resolution (640 × 480 grid points, equivalent
397 to a horizontal resolution of 40 km at mid-latitudes), which is itself initialised by ERA-Interim
398 atmospheric reanalysis (Dee et al., 2011). The model is used to provide a series of 12 to 24
399 hr forecasts, provided every 12 hrs, for the period 20151231T1200Z to 20171230T0000Z,
400 i.e. the initial 12 hrs of each forecast is discarded as spin-up. ~~We extracted a continuous~~
401 ~~forecast~~ time-series for the period November 2016 to April 2017. We extracted daily mean
402 and daily maximum near-surface diurnal air temperatures (at a height of 1.5 m above the
403 ground) for the model grid-point immediately to the ~~north~~ of Schirmacheroasen.

404

Formatted: Line spacing: Multiple 1.15 li

Deleted: is

Deleted: , with the remaining part of the forecasts concatenated together to form

Deleted: south

4 Results

4.1 Spatial Extent and Distribution of Surface Water Bodies

The seasonal evolution of meltwater bodies during the 2016-2017 summer is shown in Figure 5. The surface meltwater system transitions from a series of small isolated water bodies clustered towards the grounding line (Fig 5A), to a connected system dominated by two linear water bodies with a length of (a) ~ 20.5 km and (b) ~ 16.9 km that propagate towards the ice-shelf front (Fig 5D).

For example, on 11th December 2016, few meltwater bodies exist, and they are predominantly clustered within the blue ice region towards the grounding line in the south-west (Fig. 5A). The majority of these water bodies exist as distinct entities, and do not connect to one another. Some meltwater ponds are identified in close proximity to the nunatak. The total volume and area of all surface meltwater bodies on the 11th December is $2.8 \times 10^6 \text{ m}^3$ and $2.8 \times 10^6 \text{ m}^2$ respectively (Table 1). The mean water depth is 1.0 m, and the maximum water depth is 3.4 m (Table 1). By 17th December (Fig. 5B), there has been a marked increase in the total volume ($3.2 \times 10^7 \text{ m}^3$) and area ($4.7 \times 10^7 \text{ m}^2$) of surface meltwater, held in both circular and linear surface water bodies (Table 1). The mean water depth is 0.7 m and the maximum water depth is 3.1 m (Table 1). Several of the previously isolated ponds have coalesced in some of the main topographic lows. The spatial extent of the surface water bodies extends ~ 2 km further towards the ice-shelf front. In addition, some water bodies have begun to develop towards the eastern edge of the grounding line in a blue ice region.

A marked shift in the surface meltwater system is identified by 27th December (Fig 5C), as two large linear water bodies have formed along the north-south axis (labelled a and b in Fig. 5C). The Western linear water body (a) is ~ 6.5 km long and ~ 10 km from the Eastern linear water body (b), which is ~ 8.5 km long and proximal to the surface lakes on the ice shelf's eastern margin (Fig. 5C). Overall, there are fewer isolated lakes towards the grounding line, and the majority of the surface meltwater is proximal to the two large linear systems, at elevations of ~ 60 m to 65 m (Fig. 4). The total volume and area of all surface meltwater bodies is $4.9 \times 10^7 \text{ m}^3$ and $5.4 \times 10^7 \text{ m}^2$ respectively (Table 1). The mean water depth of all identified water bodies is 0.9 m and the maximum water depth is 4.7 m (Table 1).

By 26th January 2017 (Fig. 5D), the total volume and area of surface meltwater reaches a peak for the summer, at $5.5 \times 10^7 \text{ m}^3$ and $9.1 \times 10^7 \text{ m}^2$ respectively (Table 1). This is facilitated by the enlargement of the two large linear systems, which involves the flooding of topographic lows as water appears towards the firm further north on the ice shelf. These linear systems are now (a) ~ 20.5 km and (b) ~ 16.9 km in length, and have a mean depth of (a) 0.8 m and (b) 0.7 m. The mean depth of all water on 26th January 2017 is 0.6 m and the maximum water depth is 3.3 m (Table 1).

Formatted: Line spacing: Multiple 1.15 li

Formatted: Line spacing: Multiple 1.15 li

453 By 13th February (Fig 5E), the two large linear systems remain prominent on the ice shelf,
454 but they have lost area, depth and volume at their southern ends. The mean water depth of
455 all water is 0.6 m and the maximum water depth is 4.3 m (Table 1). The total volume and
456 area of surface meltwater bodies falls to $3.7 \times 10^7 \text{ m}^3$ and $6.3 \times 10^7 \text{ m}^2$ (Table 1), reflecting
457 the shrinkage of the two linear systems.

458 459 **4.2 Tracking Results**

460
461 Of the 1598 water bodies identified and tracked within the maximum extent matrix, 1458
462 (91%) are defined as always circular, 42 (3%) are identified as always linear, 51 (3%) are
463 defined as simple transitions, and 47 (3%) are categorised as envelopment transitions.
464 Water bodies that are always circular are predominantly clustered further south on the ice
465 shelf towards the grounding line, while water bodies defined as envelopment transitions are
466 found further north, towards the ice-shelf front (Fig. 6).

467 468 **4.2.1 Total Area and Volume of Tracked Surface Water Bodies**

469
470 For each of the tracked water body categories, Table 2 shows the maximum area and
471 volume, and the corresponding dates on which these maxima were reached. The minimum
472 area and volume for all tracked categories is zero on 14th November 2016, as no deep
473 surface melt water was detected on that date. Although 91% of water bodies identified are
474 classified as circular, they do not dominate the total area or volume of surface meltwater
475 (Fig. 7). Conversely, the envelopment transitions, of which there are only 47 in total, peak
476 at $8.0 \times 10^7 \text{ m}^2$ in area and $4.5 \times 10^7 \text{ m}^3$ in volume on 26th January 2017, over a month later
477 than the peaks in area and volume recorded for the other three categories. These
478 envelopment transitions dominate the total area and volume signals for 'all water bodies',
479 which also reach their maxima on 26th January (Table 2, Fig. 7). Between 17th December
480 2016 and 27th December 2016 'all water bodies' are effectively deepening, as their mean
481 depth increases whilst the total area increases, whereas between the 27th December and
482 the 26th January 'all water bodies' are effectively spreading, as their mean depth decreases
483 whilst total area increases. (Table 1, Fig. 7).

484 485 486 **4.2.2 Tracking Individual Water Bodies**

487
488 In addition to quantifying total surface water area and volume for each of the four water body
489 categories (Fig. 7), the FASTISh algorithm also tracks changes in the area and volume of
490 individual water bodies. Over the 2016-2017 melt season, the two largest envelopment
491 transitions, referred to as the Western System (WS) and the Eastern System (ES) hereafter,
492 propagate towards the ice-shelf front as the melt season progresses, and contain 62.6 % of
493 the total surface water volume on 26th January 2017. The remainder of this sub-section
494 focuses solely on presenting the tracking results for these two water bodies.

Deleted: Table 2,

Deleted: (Table 2)

Deleted: Between 17th December 2016 and 27th December 2016 'all water bodies' are characterised by 'deepening', as their total volume increases at a greater rate than their total area, and their mean depth increases (Tables 1 and 2, Fig. 7). Whereas between the 27th December and the 26th January, 'all water bodies' are characterised by 'spreading', as their total area increases at a faster rate than their total volume, and the mean water body depth decreases (Tables 1 and 2, Fig. 7). ...

Deleted: , Table 2

509 The WS is active between 11th December 2016 to 25th February 2017. The area and volume
510 of meltwater within the WS reaches a maximum of $4.6 \times 10^7 \text{ m}^2$ and $2.5 \times 10^7 \text{ m}^3$ respectively
511 on 26th January 2017 (Fig. 8). The ES has a shorter lifespan, and is active between 27th
512 December 2016 and 25th February 2017 (Fig. 8). The area and volume of the ES peaks at
513 $1.9 \times 10^7 \text{ m}^2$ and $9.6 \times 10^6 \text{ m}^3$ on the 26th January 2017. Figure 9 shows the surface
514 elevation profiles for the WS and the ES, which are extracted from the maximum extent
515 mask (see section 3.5). Both systems are characterised by a surface sloping downwards
516 towards the ice-shelf front. The WS has a very shallow slope, with the elevation decreasing
517 by $\sim 2 \text{ m}$ over the 25.7 km profile (Fig. 9a); the ES is slightly steeper, showing a $\sim 7.4 \text{ m}$
518 decrease in elevation over its 27 km profile (Fig. 9b).

Deleted: 6

519 520 **4.2.3 Identifying Individual Lake Freeze Through/Drainage Events.** 521

522 Previous studies have attempted to identify rapid drainage events, defined as events where
523 lakes lose $> 80 \%$ of their maximum volume in \leq four days (e.g. Fitzpatrick et al., 2014; Miles
524 et al., 2017; Williamson et al., 2018b). Here, however, the temporal resolution of available
525 imagery for the Nivlisen Ice Shelf is not high enough to allow this. Therefore, we used the
526 calculated volume time series to identify water bodies in the 'always circular' category that
527 lost $> 80 \%$ of their maximum volume over the full melt season, through either drainage or
528 freeze through. We focus solely on the 'always circular' category to better understand the
529 local loss of surface melt water in seemingly isolated and stationary water bodies. These
530 events are referred to as 'loss events' hereafter.

Formatted: Line spacing: Multiple 1.15 li

531
532 Figure 10 shows the loss in water volume through freeze-through or drainage for the 'always
533 circular' category over the melt season, together with the seven day moving average for the
534 mean daily and daily maximum near-surface air temperatures over the ice shelf from the
535 MetUM simulation. This shows that 805 lakes have a 'loss event' by 18th December 2017,
536 losing a total volume of $1.5 \times 10^7 \text{ m}^3$, which occurs following sustained relatively warmer
537 atmospheric conditions since the beginning of December 2016, e.g. characterised by daily
538 maximum near-surface air temperatures reaching 0°C .

539 540 **5 Discussion**

541 542 **5.1 Spatial and Temporal Distribution of Surface Meltwater Bodies** 543

544 In the early melt season, surface meltwater on the Nivlisen Ice Shelf ponds in small surface
545 lakes that form in relatively flat areas towards the grounding line, in close proximity to
546 Shirmacheroasen and the blue ice regions (Figs. 4 and 5). This initial generation of surface
547 meltwater is likely driven by regional wind patterns and the effects of local ice-albedo, as the
548 relatively low albedo of the blue ice can lead to increased local melt rates (Lenaerts et al.,
549 2017; Bell et al., 2018; Stokes et al., 2019). Furthermore, areas of lower elevation towards
550 the grounding line are likely to be exposed to katabatic winds, which can result in near-
551 surface temperatures that are 3 K greater than temperatures further up-ice and down-ice
552 (Lenaerts et al. 2017). These persistent katabatic winds can also result in the production of

554 blue ice regions, as snow is eroded from the ice-shelf surface (Lenaerts et al., 2017). Our
555 results for the early melt season on the Nivlisen Ice Shelf therefore support the findings of
556 Kingslake et al. (2017) who found, for a variety of ice shelves around Antarctica, that 50 %
557 of the ice-shelf drainage systems are either within 8 km of rock exposures, or within 3.6 km
558 of blue ice surfaces.

559
560 Seasonal variations in the amount of surface meltwater on the Nivlisen Ice Shelf are driven
561 by temperature fluctuations, with increases in surface water area and volume corresponding
562 with rising mean daily near-surface temperatures and daily maximum near-surface
563 temperatures (Fig. 10). However, as the melt season progresses, there is a transition to a
564 connected surface drainage network, which facilitates a progressive transfer of surface
565 meltwater away from the grounding line towards the ice-shelf front. As mean daily and daily
566 maximum temperatures rise and surface water bodies increase in area and volume (Fig.10),
567 they grow, merge with nearby water bodies, and form new extended networks of surface
568 water on the ice-shelf surface. While rising near-surface temperatures are a strong control
569 on the amount of surface meltwater, the direction and extent of the identified lateral water
570 transfer is controlled by the ice shelf's surface topography (Fig. 4b). Over the course of the
571 melt season, the area and volume of surface meltwater decreases in the regions close to
572 the grounding line, and increases in more distal parts of the ice shelf.

573
574 The development of the two largest enveloping water bodies (WS and ES) dominate the
575 transition to a generally more connected drainage network. This is because these systems
576 facilitate large-scale transfer of water across the shelf, as water ponds within linear
577 depressions. The ES and WS appear to be fed by smaller circular and linear surface
578 meltwater bodies, and as the area and volume of the ES and WS increases, they spread
579 and envelope nearby water bodies. Smaller water bodies likely contribute surface melt to
580 the ES and WS by (i) overtopping their local basin sides and flowing over impermeable ice,
581 which may be refrozen surface or shallow subsurface meltwater from previous years
582 (Kingslake et al., 2015) or (ii) percolating into the firn pack and spreading laterally towards
583 the ES and WS. However, the 'pulse' forward of the ES and WS between 27th December
584 2016 and 26th January 2017 does not appear to be ~~due to a breach of a topographic 'lip' or~~
585 'dam' (Fig. 9). It is therefore likely to primarily be the result of increased meltwater
586 production, resulting in saturation of the surrounding firn pack, which may bring it up to
587 isothermal conditions, thereby facilitating further melt and lateral transfer.

588
589 By 26th January 2017, the ES and WS are the dominant features within the entire Nivlisen
590 Ice Shelf meltwater system, together holding 62.6% of the surface meltwater volume. On
591 this date, the ES and WS reach a length of ~ 16.9 km and ~ 20.5 km respectively,
592 although unlike observations on the Nansen Ice Shelf (Bell et al., 2017), they do not
593 facilitate the export of surface meltwater off the ice-shelf front via a waterfall. Instead, both
594 systems always terminate at least ~ 35 – 55 km from the ice-shelf front, suggesting that
595 the water percolates into the surrounding firn in that area of the ice shelf. This interpretation
596 is supported by Figure 11 which shows a Sentinel-1 SAR image (Fig 11b), from 26th
597 January 2017 together with the Sentinel-2 image (Fig 11a). Areas of low backscatter

Deleted: controlled by

Formatted: Line spacing: Multiple 1.15 li

699 (appearing as dark areas in [Figure 11b](#)), extend across the grounding line onto the upper
600 part of the ice shelf. Whilst areas of low backscatter may result from [relatively small dry-](#)
601 [snow grain sizes, shallow dry-snow depths to underlying rougher surfaces, high surface](#)
602 [roughnesses, or complex internal stratigraphies](#), (Rott and Mätzler, 1987; Sun et al., 2015),
603 it seems more likely that areas of low backscatter north of the blue ice areas represent
604 saturated firn and/or surface melt (Bindschadler and Vornberger, 1992; Miles et al., 2017).
605 Areas of low backscatter clearly extend beyond areas of visible surface melt in the optical
606 imagery, indicating the presence of subsurface meltwater. For example, there are
607 prominent areas of low backscatter (~ - 5 to -15 dB) extending ~ 10 km north of both the
608 ES and WS as detected by FASTISH (Fig 11b). This shows that the linear water features
609 visible in the optical imagery are part of much larger water bodies, with a lot of the water
610 existing as slush at the surface or in the shallow subsurface.

611
612 Whilst the drainage system currently observed on the Nivlisen Ice Shelf does not transfer
613 surface meltwater all the way to the ice-shelf front, it is plausible that such a system could
614 develop in the future as the quantity of surface meltwater produced increases. Whilst the
615 water may pond, (possibly resulting in eventual hydrofracture and ice-shelf collapse), the
616 ES and WS may also evolve quickly and efficiently, over increasingly saturated firn layers,
617 to allow water to flow off the ice-shelf front, thereby exporting some excess meltwater and
618 mitigating the potential threat to the ice shelf (Bell et al., 2017; Banwell, 2017).

619
620 Overall, 1.6 % of the Nivlisen Ice Shelf is occupied by some form of surface meltwater body
621 at some point during the 2016-2017 melt season, and over those areas, the mean water
622 depth is 0.85 m. Comparatively, prior to its collapse, 5.3 % the Larsen B Ice Shelf was
623 covered by a surface meltwater body, and the mean water depth was 0.82 m (Banwell et
624 al., 2014). Whilst the mean water body depths between the Larsen B and Nivlisen Ice
625 Shelves are comparable, the spatial distributions of these water bodies, and the proportion
626 of the ice shelf that they cover, are different. Surface water bodies were distributed relatively
627 evenly across the entire surface of Larsen B before it collapsed, whereas surface water
628 bodies are predominantly clustered towards the grounding line on the Nivlisen Ice Shelf, and
629 the transfer of surface melt towards the ice-shelf front and across snow/ firn-covered regions
630 is predominantly facilitated by the larger WS and ES. The development of these large, linear
631 water bodies is likely facilitated by [ice-shelf surface](#) topography, and allows the transfer of
632 summer meltwater towards the ice-shelf front. This large scale lateral transfer of meltwater
633 is [likely](#) further facilitated as the ES and WS develop over frozen meltwater paths from
634 previous years (Kingslake et al., 2015).

635 636 **5.2 Loss of Water Volume from Circular Surface Water Bodies**

637
638 The loss of $1.5 \times 10^7 \text{ m}^3$ of surface water from the circular water bodies by 27th December
639 2017 follows sustained relatively warmer atmospheric conditions since the beginning of
640 December 2017 (Fig. 10), and coincides with an increase in the total surface water volume
641 on the ice shelf (Fig 10b). In particular, we see an increase in the volume of water held within
642 the enveloping water bodies, which continues to increase up to a maximum of $4.5 \times 10^7 \text{ m}^3$

Deleted: the image

Deleted: are widespread across the tributary glaciers and ...

Deleted: snow grain-size, surface topography/roughness, and internal stratigraphy

648 on 26th January 2017 (Fig. 7). It is likely, therefore, that the loss of water from circular water
649 bodies at this early stage in the melt season signifies the lateral transfer of water away from
650 the small 'isolated' bodies near the grounding line into the large enveloping water bodies
651 which hold and transport the surface meltwater across the ice shelf to more distal regions.
652 This lateral transfer of water may be occurring through two mechanisms: (i) the over-topping
653 of surface lakes, which results in the formation of shallow channels that connect water
654 bodies and facilitate the transfer of water towards the ice-shelf front (e.g. Banwell et al.,
655 2019), or (ii) the gradual percolation of surface meltwater into the cold firn pack, which
656 reduces the firn air content (FAC) of a region (Lenaerts et al., 2017), therefore creating an
657 impermeable surface over which water can flow (e.g. Kingslake et al., 2015). The firn may
658 also become saturated enough to be isothermal, therefore melting and facilitating the flow
659 of upstream ponded meltwater. This is particularly likely to occur near surface depressions
660 such as those that are later occupied by the WS and ES.

661

662 **5.3 Potential Implications for Ice-Shelf Stability**

663 It is expected that the area of coverage and volume of surface meltwater on Antarctic ice
664 shelves will increase into the future, in line with rising atmospheric temperatures (Bell et
665 al., 2018; IPCC, 2019; Kingslake et al., 2017; Siegert et al., 2019). This surface water may
666 have significant implications for ice-shelf stability, as meltwater accumulation can lead to
667 hydrofracture which could subsequently result in the collapse of an ice shelf, as seen on
668 the Larsen B Ice Shelf in 2002 (Robel and Banwell, 2019; Banwell et al., 2013). An ice
669 shelf may become increasingly vulnerable to hydrofracture if its FAC is reduced (Lenaerts
670 et al., 2017). On ice shelves like Nivlisen, where large-scale lateral water transfer prevails,
671 meltwater is delivered to locations that may otherwise not receive or experience much melt
672 (Bell et al., 2017), and the FAC of these locations will, in turn, be reduced, increasing their
673 susceptibility to surface meltwater ponding and hydrofracture.

674 Surface meltwater re-freezing at the end of the melt season will also act as a significant
675 source of heat, and the lateral transfer of surface melt could cause increased warming of
676 the ice shelf and possible weakening in areas which currently do not experience significant
677 summer melt. Were the maximum volume of surface meltwater we observe on the Nivlisen
678 Ice Shelf in the 2016-2017 melt season ($5.5 \times 10^7 \text{ m}^3$) to re-freeze over the maximum area
679 of surface meltwater ($9.1 \times 10^7 \text{ m}^2$), it would release an amount of energy equivalent to 49
680 days of potential solar energy receipts (calculated using the methods of Arnold and Rees
681 (2009)), assuming an ice surface albedo of 0.86; the mean value calculated for a water-
682 free distal area of the ice shelf. Furthermore, large-scale lateral water transfer and
683 subsequent ponding may lead to ice-shelf flexure (and therefore potential fracture) at
684 locations that may have otherwise not been affected by flexure in response to meltwater
685 loading (Banwell et al., 2013, 2019; Macayeal and Sergienko, 2013). However, evidence
686 of lateral water transfer and export off the Nansen Ice Shelf has highlighted the potential
687 for surface drainage systems to mitigate some of these meltwater-driven instabilities (Bell
688 et al., 2017).

Deleted:

690
691
692
693
694
695
696
697
698
699
700
701
702
703
704
705
706
707
708
709
710
711
712
713
714
715
716
717
718
719
720
721
722
723
724
725
726
727
728
729
730
731
732
733

6 Conclusions

We have adapted the pre-existing FASTER algorithm, developed for studying lakes on the GrIS (Williamson et al., 2018b), so that we can identify and track the area, depth and volume of water bodies across Antarctic ice shelves. We refer to this new algorithm as FASTISH, and have used it to study the changing geometry and spatial patterns of water bodies across the Nivlisen Ice Shelf in the 2016-2017 melt season. In total, we identify and track 1598 water bodies on the ice shelf over the course of the melt season. Surface water is initially generated towards the nunatak and blue ice region, in proximity to the grounding line. This region is relatively flat and has a low albedo, and we therefore observe localised ponding of surface meltwater. As the melt season progresses and mean daily and daily maximum temperatures increase, we see a transition from isolated, localised ponding towards the grounding line to a more connected drainage system that is influenced by the ice-shelf topography. The middle of the melt season (e.g. 27th December 2016) is characterised by the progression of surface melt water bodies towards the ice-shelf front, as two large extensive drainage systems (the East System (ES) and West System (WS)) develop in long linear surface depressions. Around the peak of the melt season (26th January 2017), the ES and WS have developed to their largest observed extent, and facilitate the lateral transfer of surface melt up to 16.9 and 20.5 km north, into the firn pack and towards the ice-shelf front. The transfer of surface meltwater to regions on the ice shelf that otherwise experience little surface melt may have implications for the structure and stability of the ice shelf in the future. Our findings could be useful in comparing to IceSat 2 derived lake depths (Fair et al., 2020), in addition to constraining ice-shelf surface hydrology models (Buzzard et al., 2018).

Code and Data Availability

The satellite imagery, REMA data, and meteorological data are all open access (see section 3). The MATLAB scripts used to process the data will be freely available from Apollo Repository (<https://www.repository.cam.ac.uk/>) upon publication.

Author Contributions

RLD developed the methodology and scripts, building on the prior work of AGW. NSA developed the script to convert Landsat DN values to per-pixel TOA values. AO performed the Regional Climate Model run using the Met Office Unified Model to provide the meteorological data. RLD conducted all other analysis and wrote the draft manuscript, under the supervision of all other authors. All authors discussed the results and were involved in editing of the manuscript.

Competing Interests

The authors declare no competing interests

Formatted: Font colour: Text 1

Deleted: future

Formatted: Line spacing: Multiple 1.15 li

Deleted: <https://www.repository.cam.ac.uk/>

736 **Acknowledgements**

737
738 We sincerely thank Mahsa Moussavi and Allen Pope for their guidance and many productive
739 discussions over the past two years. Rebecca Dell acknowledges support from a Natural
740 Environment Research Council Doctoral Training Partnership Studentship (Grant number:
741 NE/L002507/1; CASE Studentship with the British Antarctic Survey). Ian Willis
742 acknowledges support from NERC Grant G102130. This paper was written while Ian Willis
743 was in receipt of a Cooperative Institute for Research in Environmental Science (CIRES)
744 Visiting Sabbatical Fellowship and he thanks in particular Waleed Abdalati, Ted Scambos,
745 Kristy Tiampo and Mike Willis for their hospitality. Alison Banwell acknowledges support
746 from a CIRES Visiting Postdoctoral Fellowship and a grant from the US National Science
747 Foundation (#1841607) awarded to the University of Colorado, Boulder. AO thanks Tony
748 Phillips (BAS) for converting the MetUM output to daily averaged fields. DEMs provided by
749 the Byrd Polar and Climate Research Center and the Polar Geospatial Center under
750 NSF-OPP awards 1543501, 1810976, 1542736, 1559691, 1043681, 1541332,
751 0753663, 1548562, 1238993 and NASA award NNX10AN61G. Computer time
752 provided through a Blue Waters Innovation Initiative. DEMs produced using data from
753 DigitalGlobe, Inc.

754
755
756 **References**

- 757
758 Arnold, N. and Rees, G.: Effects of digital elevation model spatial resolution on distributed
759 calculations of solar radiation loading on a high arctic glacier, *J. Glaciol.*, 55(194), 973–
760 984, doi:10.3189/002214309790794959, 2009.
- 761 Arnold, N. S., Banwell, A. F. and Willis, I. C.: High-resolution modelling of the seasonal
762 evolution of surface water storage on the Greenland Ice Sheet, *Cryosph.*, 8(4), 1149–
763 1160, doi:10.5194/tc-8-1149-2014, 2014.
- 764 Arthur, J., Stokes, C., Jamieson, S., Carr, J. and Leeson, A.: Recent understanding of
765 Antarctic supraglacial lakes using satellite remote sensing., *Prog. Phys. Geogr.*,
766 030913332091611, doi:10.1177/0309133320916114, 2020.
- 767 Banwell, A.: Glaciology: Ice-shelf stability questioned, *Nature*, 544(7650), 306–307,
768 doi:10.1038/544306a, 2017.
- 769 Banwell, A. F. and MacAyeal, D. R.: Ice-shelf fracture due to viscoelastic flexure stress
770 induced by fill/drain cycles of supraglacial lakes, *Antarct. Sci.*, 27(6), 587–597,
771 doi:10.1017/S0954102015000292, 2015.
- 772 Banwell, A. F., MacAyeal, D. R. and Sergienko, O. V.: Breakup of the Larsen B Ice Shelf
773 triggered by chain reaction drainage of supraglacial lakes, *Geophys. Res. Lett.*, 40(22),
774 5872–5876, doi:10.1002/2013GL057694, 2013.
- 775 Banwell, A. F., Caballero, M., Arnold, N. S., Glasser, N. F., Cathles, L. Mac and MacAyeal,
776 D. R.: Supraglacial lakes on the Larsen B ice shelf, Antarctica, and at Paakitsoq, West
777 Greenland: A comparative study, *Ann. Glaciol.*, 55(66), 1–8,
778 doi:10.3189/2014AoG66A049, 2014.
- 779 Banwell, A. F., Willis, I. C., Macdonald, G. J., Goodsell, B. and MacAyeal, D. R.: Direct

Formatted: Line spacing: Multiple 1.15 li

Formatted: Line spacing: Multiple 1.15 li

780 measurements of ice-shelf flexure caused by surface meltwater ponding and drainage,
781 *Nat. Commun.*, 10(1), 1–10, doi:10.1038/s41467-019-08522-5, 2019.

782 Bell, R. E., Chu, W., Kingslake, J., Das, I., Tedesco, M., Tinto, K. J., Zappa, C. J.,
783 Frezzotti, M., Boghosian, A. and Lee, W. S.: Antarctic ice shelf potentially stabilized by
784 export of meltwater in surface river, *Nature*, 544(7650), 344–348,
785 doi:10.1038/nature22048, 2017.

786 Bell, R. E., Banwell, A. F., Trusel, L. D. and Kingslake, J.: Antarctic surface hydrology and
787 impacts on ice-sheet mass balance, *Nat. Clim. Chang.*, 8(12), 1044–1052,
788 doi:10.1038/s41558-018-0326-3, 2018.

789 Bevan, S. L., Luckman, A., Hubbard, B., Kulesa, B., Ashmore, D., Kuipers Munneke, P.,
790 O’Leary, M., Booth, A., Sevestre, H. and McGrath, D.: Centuries of intense surface melt on
791 Larsen C Ice Shelf, *Cryosphere*, 11(6), 2743–2753, doi:10.5194/tc-11-2743-2017, 2017.

792 Bindschadler, R. and Vornberger, P.: Interpretation of sar imagery of the greenland ice
793 sheet using coregistered TM imagery, *Remote Sens. Environ.*, 42(3), 167–175,
794 doi:10.1016/0034-4257(92)90100-X, 1992.

795 Bush, M., Allen, T., Bain, C., Boutle, I., Edwards, J., Finnenkoetter, A., Franklin, C.,
796 Hanley, K., Lean, H., Lock, A., Manners, J., Mittermaier, M., Morcrette, C., North, R.,
797 Petch, J., Short, C., Vosper, S., Walters, D., Webster, S., Weeks, M., Wilkinson, J., Wood,
798 N. and Zerroukat, M.: The first Met Office Unified Model/JULES Regional Atmosphere and
799 Land configuration, RAL1, *Geosci. Model Dev. Discuss.*, 1–47, doi:10.5194/gmd-2019-
800 130, 2019.

801 Buzzard, S., Feltham, D. and Flocco, D.: Modelling the fate of surface melt on the Larsen
802 C Ice Shelf, *Cryosphere*, 12(11), 3565–3575, doi:10.5194/tc-12-3565-2018, 2018.

803 Cook, A. J. and Vaughan, D. G.: Overviewing of areal changes of the ice shelves on the
804 Antarctic Peninsula over the past 50 years, *Cryosph.*, 4, 77–98 [online] Available from:
805 <http://dro.dur.ac.uk/20037/1/20037.pdf> (Accessed 7 June 2018), 2010.

806 Datta, R. T., Tedesco, M., Fettweis, X., Agosta, C., Lhermitte, S., Lenaerts, J. T. M. and
807 Wever, N.: The Effect of Foehn-Induced Surface Melt on Firn Evolution Over the Northeast
808 Antarctic Peninsula, *Geophys. Res. Lett.*, 46(7), 3822–3831, doi:10.1029/2018GL080845,
809 2019.

810 DeConto, R. M. and Pollard, D.: Contribution of Antarctica to past and future sea-level rise,
811 *Nature*, 531(7596), 591–597, doi:10.1038/nature17145, 2016.

812 Dee, D. P., Uppala, S. M., Simmons, A. J., Berrisford, P., Poli, P., Kobayashi, S., Andrae,
813 U., Balmaseda, M. A., Balsamo, G., Bauer, P., Bechtold, P., Beljaars, A. C. M., van de
814 Berg, L., Bidlot, J., Bormann, N., Delsol, C., Dragani, R., Fuentes, M., Geer, A. J.,
815 Haimberger, L., Healy, S. B., Hersbach, H., Hólm, E. V., Isaksen, L., Kållberg, P., Köhler,
816 M., Matricardi, M., McNally, A. P., Monge-Sanz, B. M., Morcrette, J. J., Park, B. K.,
817 Peubey, C., de Rosnay, P., Tavolato, C., Thépaut, J. N. and Vitart, F.: The ERA-Interim
818 reanalysis: Configuration and performance of the data assimilation system, *Q. J. R.*
819 *Meteorol. Soc.*, 137(656), 553–597, doi:10.1002/qj.828, 2011.

820 Dow, C. F., Lee, W. S., Greenbaum, J. S., Greene, C. A., Blankenship, D. D., Poinar, K.,
821 Forrest, A. L., Young, D. A. and Zappa, C. J.: Basal channels drive active surface
822 hydrology and transverse ice shelf fracture, *Sci. Adv.*, 4(6), eaao7212,
823 doi:10.1126/sciadv.aao7212, 2018.

824 Echelmeyer, K., Clarke, T. S. and Harrison, W. D.: Surficial glaciology of Jakobshavns
825 Isbrae, West Greenland: part I. Surface morphology, *J. Glaciol.*, 37(127), 368–382,
826 doi:10.1017/S0022143000005803, 1991.

827 Fair, Z., Flanner, M., Brunt, K., Fricker, H. A. and Gardner, A.: Using ICESat-2 and
828 Operation IceBridge altimetry for supraglacial lake depth retrievals, *Cryosph. Discuss.*,
829 doi:10.5194/tc-2020-136, [in review](#), 2020.

830 Fitzpatrick, A. A. W., Hubbard, A. L., Box, J. E., Quincey, D. J., Van As, D., Mikkelsen, A.
831 P. B., Doyle, S. H., Dow, C. F., Hasholt, B. and Jones, G. A.: A decade (2002-2012) of
832 supraglacial lake volume estimates across Russell Glacier, West Greenland, *Cryosphere*,
833 8(1), 107–121, doi:10.5194/tc-8-107-2014, 2014.

834 Fürst, J. J., Durand, G., Gillet-Chaulet, F., Tavad, L., Rankl, M., Braun, M. and
835 Gagliardini, O.: The safety band of Antarctic ice shelves, *Nat. Clim. Chang.*, 6(5), 479–482,
836 doi:10.1038/nclimate2912, 2016.

837 Glasser, N. F. and Gudmundsson, G. H.: Longitudinal surface structures (flowstripes) on
838 Antarctic glaciers, *Cryosphere*, 6(2), 383–391, doi:10.5194/tc-6-383-2012, 2012.

839 Glasser, N. F. and Scambos, T. A.: A structural glaciological analysis of the 2002 Larsen B
840 ice-shelf collapse, *J. Glaciol.*, 54(184), 3–16, doi:10.3189/002214308784409017, 2008.

841 Gudmundsson, G. H., Paolo, F. S., Adusumilli, S. and Fricker, H. A.: Instantaneous
842 Antarctic ice-sheet mass loss driven by thinning ice shelves, *Geophys. Res. Lett.*,
843 2019GL085027, doi:10.1029/2019GL085027, 2019.

844 Hall, D. K., Branch, H. S., Tait, A. B., Riggs, G. A., Corporation, D. S., Salomonson, V. V.,
845 Directorate, E. S., Chien, J. Y. L., Corporation, G. S. and Klein, A. G.: Algorithm
846 Theoretical Basis Document (ATBD) for the MODIS Snow-, Lake Ice- and Sea Ice-
847 Mapping Algorithms, Analysis [online] Available from:
848 https://eosps0.gsfc.nasa.gov/sites/default/files/atbd/atbd_mod10.pdf (Accessed 21 April
849 2019), 2001.

850 Horwath, M., Dietrich, R., Baessler, M., Nixdorf, U., Steinhage, D., Fritzsche, D., Damm, V.
851 and Reitmayr, G.: Nivlisen, an Antarctic ice shelf in Dronning Maud Land: Geodetic-
852 glaciological results from a combined analysis of ice thickness, ice surface height and ice-
853 flow observations, *J. Glaciol.*, 52(176), 17–30, doi:10.3189/172756506781828953, 2006.

854 Howat, I. M., Porter, C., Smith, B. E., Noh, M. J. and Morin, P.: The reference elevation
855 model of antarctica, *Cryosphere*, 13(2), 665–674, doi:10.5194/tc-13-665-2019, 2019.

856 Hubbard, B., Luckman, A., Ashmore, D. W., Bevan, S., Kulesa, B., Kuipers Munneke, P.,
857 Philippe, M., Jansen, D., Booth, A., Sevestre, H., Tison, J. L., O’Leary, M. and Rutt, I.:
858 Massive subsurface ice formed by refreezing of ice-shelf melt ponds, *Nat. Commun.*, 7,
859 doi:10.1038/ncomms11897, 2016.

860 Hui, F., Ci, T., Cheng, X., Scambos, T. A., Liu, Y., Zhang, Y., Chi, Z., Huang, H., Wang, X.,
861 Wang, F., Zhao, C., Jin, Z. and Wang, K.: Mapping blue-ice areas in Antarctica using
862 ETM+ and MODIS data, *Ann. Glaciol.*, 55(66), 129–137, doi:10.3189/2014AoG66A069,
863 2014.

864 IPCC: Special Report on the Ocean and Cryosphere in a Changing Climate - Technical
865 Summary (Final Draft). [online] Available from: <https://www.ipcc.ch/srocc/> (Accessed 18
866 December 2019), 2019.

867 Kingslake, J., Ng, F. and Sole, A.: Modelling channelized surface drainage of supraglacial

868 lakes, *J. Glaciol.*, 61(225), 185–199, doi:10.3189/2015JoG14J158, 2015.

869 Kingslake, J., Ely, J. C., Das, I. and Bell, R. E.: Widespread movement of meltwater onto
870 and across Antarctic ice shelves, *Nature*, 544(7650), 349–352, doi:10.1038/nature22049,
871 2017.

872 Koziol, C., Arnold, N., Pope, A. and Colgan, W.: Quantifying supraglacial meltwater
873 pathways in the Paakitsoq region, West Greenland, *J. Glaciol.*, 63(239), 464–476,
874 doi:10.1017/jog.2017.5, 2017.

875 Kuipers Munneke, P., Ligtenberg, S. R. M., Van Den Broeke, M. R. and Vaughan, D. G.:
876 Firn air depletion as a precursor of Antarctic ice-shelf collapse, *J. Glaciol.*, 60(220), 205–
877 214, doi:10.3189/2014JoG13J183, 2014.

878 Langley, E. S., Leeson, A. A., Stokes, C. R. and Jamieson, S. S. R.: Seasonal evolution of
879 supraglacial lakes on an East Antarctic outlet glacier, *Geophys. Res. Lett.*, 43(16), 8563–
880 8571, doi:10.1002/2016GL069511, 2016.

881 Leeson, A. A., Forster, E., Rice, A., Gourmelen, N. and van Wessem, J. M.: Evolution of
882 Supraglacial Lakes on the Larsen B Ice Shelf in the Decades Before it Collapsed,
883 *Geophys. Res. Lett.*, 47(4), doi:10.1029/2019GL085591, 2020.

884 Lenaerts, J., Lhermitte, S., Drews, R., Ligtenberg, S. R. M., Berger, S., Helm, V., Smeets,
885 P. C. J. P., van den Broeke, M. R., van De Berg, W. J., van Meijgaard, E., Eijkelboom, M.,
886 Eisen, O. and Pattyn, F.: Meltwater produced by wind – albedo interaction stored in an
887 East Antarctic ice shelf, *Nat. Clim. Chang.*, 7, 58–63, doi:10.1038/NCLIMATE3180, 2017.

888 Liston, G. E. and Winther, J. G.: Antarctic surface and subsurface snow and ice melt
889 fluxes, *J. Clim.*, 18(10), 1469–1481, doi:10.1175/JCLI3344.1, 2005.

890 Liston, G. E., Winther, J. G., Bruland, O., Elvehøy, H. and Sand, K.: Below-surface ice
891 melt on the coastal Antarctic ice sheet, *J. Glaciol.*, 45(150), 273–285,
892 doi:10.3189/s0022143000001775, 1999.

893 Luckman, A., Elvidge, A., Jansen, D., Kulesa, B., Kuipers Munneke, P., King, J. and
894 Barrand, N. E.: Surface melt and ponding on Larsen C Ice Shelf and the impact of föhn
895 winds, *Antarct. Sci.*, 26(6), 625–635, doi:10.1017/S0954102014000339, 2014.

896 Macayeal, D. R. and Sergienko, O. V.: The flexural dynamics of melting ice shelves, *Ann.*
897 *Glaciol.*, 54(63), 1–10, doi:10.3189/2013AoG63A256, 2013.

898 Macdonald, G. J., Banwell, A. F. and Macayeal, D. R.: Seasonal evolution of supraglacial
899 lakes on a floating ice tongue , Petermann Glacier , Greenland , , 1–10,
900 doi:10.1017/aog.2018.9, 2018.

901 McGrath, D., Steffen, K., Rajaram, H., Scambos, T., Abdalati, W. and Rignot, E.: Basal
902 crevasses on the Larsen C Ice Shelf, Antarctica: Implications for meltwater ponding and
903 hydrofracture, *Geophys. Res. Lett.*, 39(16), n/a-n/a, doi:10.1029/2012GL052413, 2012.

904 Miles, K. E., Willis, I. C., Benedek, C. L., Williamson, A. G. and Tedesco, M.: Toward
905 Monitoring Surface and Subsurface Lakes on the Greenland Ice Sheet Using Sentinel-1
906 SAR and Landsat-8 OLI Imagery, *Front. Earth Sci.*, 5, doi:10.3389/feart.2017.00058, 2017.

907 Mottram, R., Hansen, N., Kittel, C., Wessem, M. van, Agosta, C., Amory, C., Boberg, F.,
908 Berg, W. J. van de, Fettweis, X., Gossart, A., Meijgaard, E. van, Orr, A., Phillips, T.,
909 Webster, S., Simonsen, S. and Souverijns, N.: What is the Surface Mass Balance of
910 Antarctica? An Intercomparison of Regional Climate Model Estimates, *Cryosph. Discuss.*,
911 1–42, doi:10.5194/tc-2019-333, [in review](#), 2020.

¶12 Mouginot, J., Scheuchl, B. and Rignot, E.: MEaSURES Antarctic Boundaries for IPY 2007-
 913 2009 from Satellite Radar, Version 2., NASA Natl. Snow Ice Data Cent. Distrib. Act. Arch.
 914 Center., doi:<https://doi.org/10.5067/AXE4121732AD>, 2017.

¶15 Moussavi, M. S., Abdalati, W., Pope, A., Scambos, T., Tedesco, M., MacFerrin, M. and
 916 Grigsby, S.: Derivation and validation of supraglacial lake volumes on the Greenland Ice
 917 Sheet from high-resolution satellite imagery, *Remote Sens. Environ.*, 183, 294–303,
 918 doi:[10.1016/j.rse.2016.05.024](https://doi.org/10.1016/j.rse.2016.05.024), 2016.

¶19 Philpot, W. D.: Bathymetric mapping with passive multispectral imagery, *Appl. Opt.*, 28(8),
 920 1569, doi:[10.1364/ao.28.001569](https://doi.org/10.1364/ao.28.001569), 1989.

¶21 Pope, A.: Reproducibly estimating and evaluating supraglacial lake depth with Landsat 8
 922 and other multispectral sensors, *Earth Sp. Sci.*, 3(4), 176–188,
 923 doi:[10.1002/2015EA000125](https://doi.org/10.1002/2015EA000125), 2016.

¶24 Pope, A., Scambos, T. A., Moussavi, M., Tedesco, M., Willis, M., Shean, D. and Grigsby,
 925 S.: Estimating supraglacial lake depth in West Greenland using Landsat 8 and comparison
 926 with other multispectral methods, *Cryosphere*, 10(1), 15–27, doi:[10.5194/tc-10-15-2016](https://doi.org/10.5194/tc-10-15-2016),
 927 2016.

¶28 Rignot, E., Casassa, G., Gogineni, P., Krabill, W., Rivera, A. and Thomas, R.: Accelerated
 929 ice discharge from the Antarctic Peninsula following the collapse of Larsen B ice shelf,
 930 *Geophys. Res. Lett.*, 31(18), L18401, doi:[10.1029/2004GL020697](https://doi.org/10.1029/2004GL020697), 2004.

¶31 Rignot, E., Mouginot, J., Scheuchl, B., Van Den Broeke, M., Van Wessem, M. J. and
 932 Morlighem, M.: Four decades of Antarctic ice sheet mass balance from 1979–2017, *Proc.*
 933 *Natl. Acad. Sci. U. S. A.*, 116(4), 1095–1103, doi:[10.1073/pnas.1812883116](https://doi.org/10.1073/pnas.1812883116), 2019.

¶34 Robel, A. A. and Banwell, A. F.: A Speed Limit on Ice Shelf Collapse Through
 935 Hydrofracture, *Geophys. Res. Lett.*, 46(21), 12092–12100, doi:[10.1029/2019GL084397](https://doi.org/10.1029/2019GL084397),
 936 2019.

¶37 Rott, H. and Mätzler, C.: Possibilities and Limits of Synthetic Aperture Radar for Snow and
 938 Glacier Surveying, *Ann. Glaciol.*, 9, 195–199, doi:[10.3189/s0260305500000604](https://doi.org/10.3189/s0260305500000604), 1987.

¶39 De Rydt, J., Gudmundsson, G. H., Rott, H. and Bamber, J. L.: Modeling the instantaneous
 940 response of glaciers after the collapse of the Larsen B Ice Shelf, *Geophys. Res. Lett.*,
 941 42(13), 5355–5363, doi:[10.1002/2015GL064355](https://doi.org/10.1002/2015GL064355), 2015.

¶42 Scambos, T., Hulbe, C. and Fahnestock, M.: Climate-induced ice shelf disintegration in the
 943 Antarctic Peninsula, in *Antarctica Peninsula climate variability: a historical and paleo-*
 944 *environmental perspective*, pp. 79–92., 2003.

¶45 Scambos, T., Fricker, H. A., Liu, C. C., Bohlander, J., Fastook, J., Sargent, A., Massom, R.
 946 and Wu, A. M.: Ice shelf disintegration by plate bending and hydro-fracture—Satellite
 947 observations and model results of the 2008 Wilkins ice shelf break-ups, *Earth Planet. Sci.*
 948 *Lett.*, 280ID–6, 51–60, doi:[10.1016/j.epsl.2008.12.027](https://doi.org/10.1016/j.epsl.2008.12.027), 2009.

¶49 Scambos, T. A., Bohlander, J. A., Shuman, C. A. and Skvarca, P.: Glacier acceleration
 950 and thinning after ice shelf collapse in the Larsen B embayment, Antarctica, *Geophys.*
 951 *Res. Lett.*, 31(18), L18402, doi:[10.1029/2004GL020670](https://doi.org/10.1029/2004GL020670), 2004.

¶52 Selmes, N., Murray, T. and James, T. D.: Fast draining lakes on the Greenland Ice Sheet,
 953 *Geophys. Res. Lett.*, 38(15), n/a-n/a, doi:[10.1029/2011GL047872](https://doi.org/10.1029/2011GL047872), 2011.

¶54 Selmes, N., Murray, T. and James, T. D.: Characterizing supraglacial lake drainage and
 955 freezing on the Greenland Ice Sheet, *Cryosph. Discuss.*, 7(1), 475–505, doi:[10.5194/tcd-7-](https://doi.org/10.5194/tcd-7-)

956 475-2013, 2013.

957 Sergienko, O. V.: Glaciological twins: Basally controlled subglacial and supraglacial lakes,
958 *J. Glaciol.*, 59(213), 3–8, doi:10.3189/2013JoG12J040, 2013.

959 Siegert, M., Atkinson, A., Banwell, A., Brandon, M., Convey, P., Davies, B., Downie, R.,
960 Edwards, T., Hubbard, B., Marshall, G., Rogelj, J., Rumble, J., Stroeve, J. and Vaughan,
961 D.: The Antarctic Peninsula under a 1.5°C global warming scenario, *Front. Environ. Sci.*,
962 7(JUN), doi:10.3389/fenvs.2019.00102, 2019.

963 Sneed, W. A. and Hamilton, G. S.: Evolution of melt pond volume on the surface of the
964 Greenland Ice Sheet, *Geophys. Res. Lett.*, 34(3), L03501, doi:10.1029/2006GL028697,
965 2007.

966 Sneed, W. A. and Hamilton, G. S.: Validation of a method for determining the depth of
967 glacial melt ponds using satellite imagery, *Ann. Glaciol.*, 52(59), 15–22,
968 doi:10.3189/172756411799096240, 2011.

969 Stokes, C. R., Sanderson, J. E., Miles, B. W. J., Jamieson, S. S. R. and Leeson, A. A.:
970 Widespread distribution of supraglacial lakes around the margin of the East Antarctic Ice
971 Sheet, *Sci. Rep.*, 9(1), doi:10.1038/s41598-019-50343-5, 2019.

972 Sun, S., Che, T., Wang, J., Li, H., Hao, X., Wang, Z. and Wang, J.: Estimation and
973 analysis of snow water equivalents based on C-band SAR data and field measurements,
974 *Arctic, Antarct. Alp. Res.*, 47(2), 313–326, doi:10.1657/AAAR00C-13-135, 2015.

975 Traganos, D., Poursanidis, D., Aggarwal, B., Chrysoulakis, N. and Reinartz, P.: Estimating
976 satellite-derived bathymetry (SDB) with the Google Earth Engine and sentinel-2, *Remote
977 Sens.*, 10(6), 859, doi:10.3390/rs10060859, 2018.

978 Vieli, A., Payne, A. J., Du, Z. and Shepherd, A.: Numerical modelling and data assimilation
979 of the Larsen B ice shelf, Antarctic Peninsula, *Philos. Trans. R. Soc. A Math. Phys. Eng.
980 Sci.*, 364(1844), 1815–1839, doi:10.1098/rsta.2006.1800, 2006.

981 Walters, D., Boutle, I., Brooks, M., Melvin, T., Stratton, R., Vosper, S., Wells, H., Williams,
982 K., Wood, N., Allen, T., Bushell, A., Copley, D., Earnshaw, P., Edwards, J., Gross, M.,
983 Hardiman, S., Harris, C., Heming, J., Klingaman, N., Levine, R., Manners, J., Martin, G.,
984 Milton, S., Mittermaier, M., Morcrette, C., Riddick, T., Roberts, M., Sanchez, C., Selwood,
985 P., Stirling, A., Smith, C., Suri, D., Tennant, W., Luigi Vidale, P., Wilkinson, J., Willett, M.,
986 Woolnough, S. and Xavier, P.: The Met Office Unified Model Global Atmosphere 6.0/6.1
987 and JULES Global Land 6.0/6.1 configurations, *Geosci. Model Dev.*, 10(4), 1487–1520,
988 doi:10.5194/gmd-10-1487-2017, 2017.

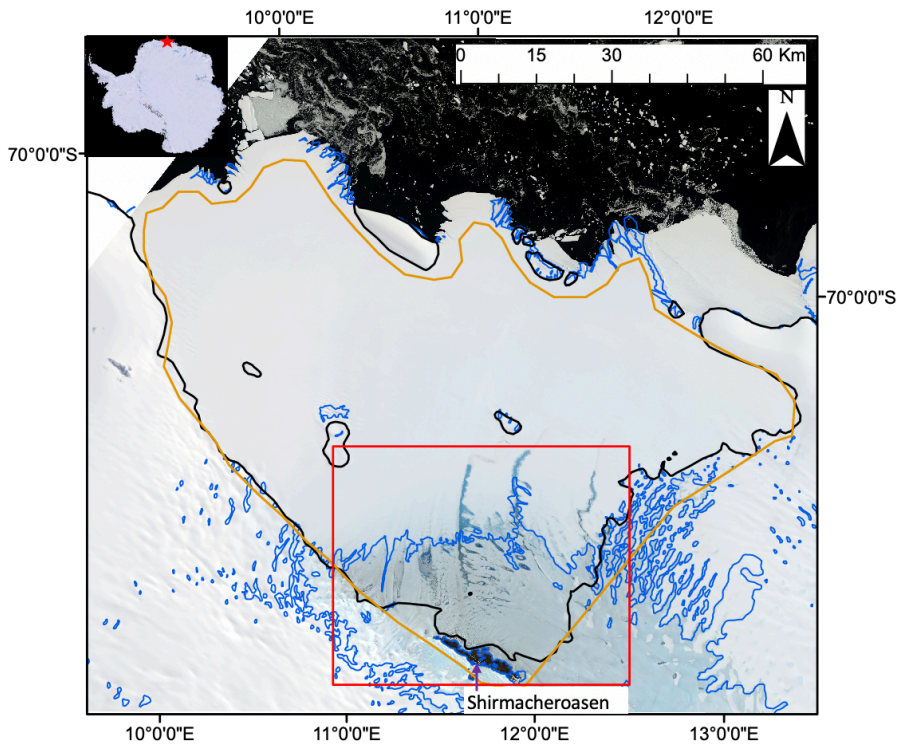
989 Williamson, A. G., Arnold, N. S., Banwell, A. F. and Willis, I. C.: A Fully Automated
990 Supraglacial lake area and volume Tracking (“FAST”) algorithm: Development and
991 application using MODIS imagery of West Greenland, *Remote Sens. Environ.*, 196, 113–
992 133, doi:10.1016/j.rse.2017.04.032, 2017.

993 Williamson, A. G., Willis, I. C., Arnold, N. S. and Banwell, A. F.: Controls on rapid
994 supraglacial lake drainage in West Greenland: an Exploratory Data Analysis approach, *J.
995 Glaciol.*, 1–19, doi:10.1017/jog.2018.8, 2018a.

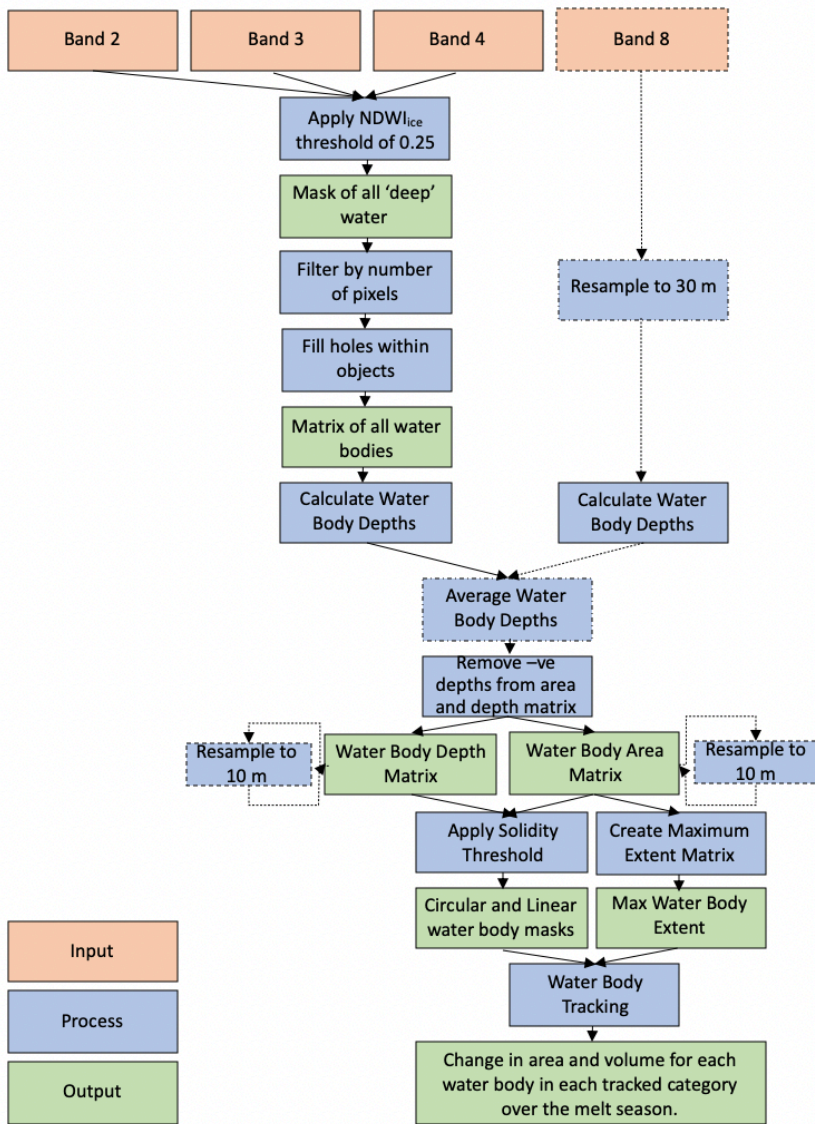
996 Williamson, A. G., Banwell, A. F., Willis, I. C. and Arnold, N. S.: Dual-satellite (Sentinel-2
997 and Landsat 8) remote sensing of supraglacial lakes in Greenland, *Cryosph. Discuss.*, 1–
998 27, doi:10.5194/tc-2018-56, 2018b.

999 Winther, J.-G. G., Elvehøy, H., Bøggild, C. E., Sand, K. and Liston, G.: Melting, runoff and

1000 the formation of frozen lakes in a mixed snow and blue-ice field in Dronning Maud Land,
1001 Antarctica, *J. Glaciol.*, 42(141), 271–278, doi:10.3189/s0022143000004135, 1996.
1002 Wuite, J., Rott, H., Hetzenecker, M., Floricioiu, D., De Rydt, J., Gudmundsson, G. H.,
1003 Nagler, T. and Kern, M.: Evolution of surface velocities and ice discharge of Larsen B
1004 outlet glaciers from 1995 to 2013, *Cryosphere*, 9(3), 957–969, doi:10.5194/tc-9-957-2015,
1005 2015.
1006 Yang, K. and Smith, L. C.: Supraglacial streams on the Greenland Ice Sheet delineated
1007 from combined spectral – shape information in high-resolution satellite imagery, *IEEE*
1008 *Geosci. Remote Sens. Lett.*, 10(4), 801–805, doi:10.1109/LGRS.2012.2224316, 2013.
1009
1010
1011
1012
1013
1014
1015
1016
1017
1018
1019
1020
1021
1022
1023
1024
1025



1026
 1027
 1028 *Figure 1: A map of the study area. The base image is a mosaicked RGB Sentinel-2 image of the*
 1029 *Nivlisen Ice Shelf acquired on 26th January 2017. The solid black line marks the grounding line,*
 1030 *according to the NASA Making Earth System Data Records for Use in Research Environments*
 1031 *(MEaSUREs) Antarctic boundaries dataset (Mouginot et al., 2017). The solid blue line represents*
 1032 *the blue ice areas in the region according to Hui et al. (2014). The solid orange line*
 1033 *roughly delineates the ice shelf and shows the study area extent used for this study, and the solid red line marks the*
 1034 *area shown in all subsequent figures. The red star on the inset shows the location of the Nivlisen Ice*
 1035 *Shelf in the context of an image of Antarctica, which is a mosaic product based on sources from*
 1036 *USGS, NASA, National Science Foundation, and the British Antarctic Survey*
 1037 *(<https://visibleearth.nasa.gov/view.php?id=78592>).*
 1038
 1039
 1040



1041

1042

1043

1044

1045

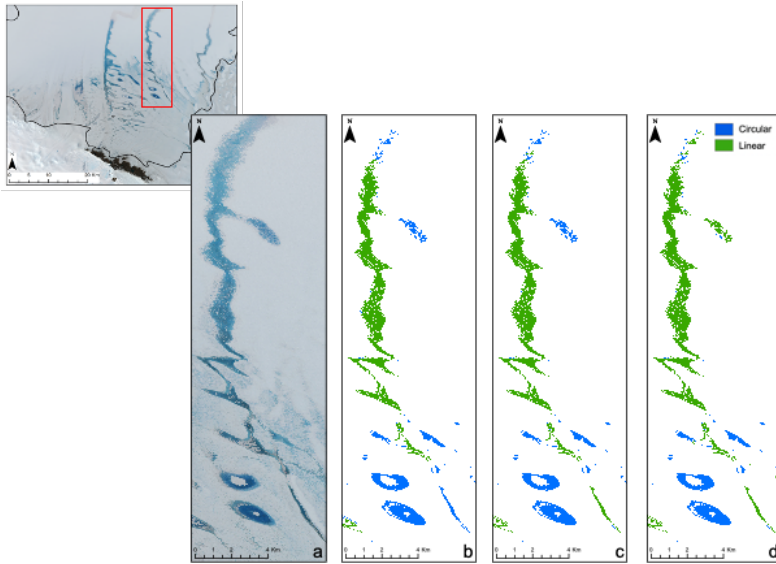
1046

1047

1048

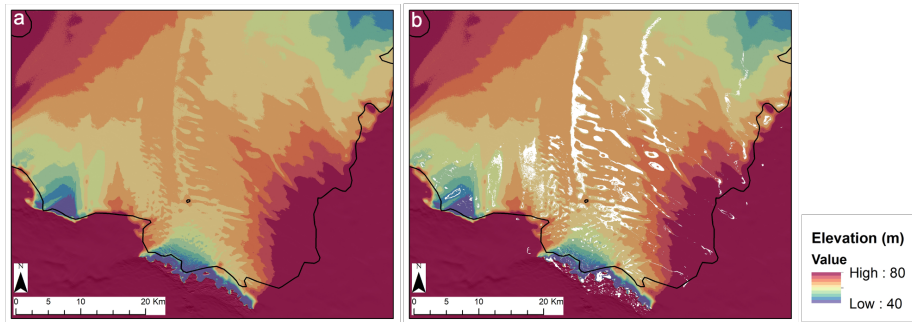
Figure 2: Workflow detailing the methods applied to both the Landsat 8 and Sentinel-2 images through the FASTISH algorithm in MATLAB. Dashed lines indicate steps that were applied to Landsat 8 images only, whereas solid lines indicate steps that were applied to both sets of image types. Modified from Williamson et al. (2018b).

Formatted: Line spacing: Multiple 1.15 li



1049
1050
1051
1052
1053
1054
1055
1056
1057

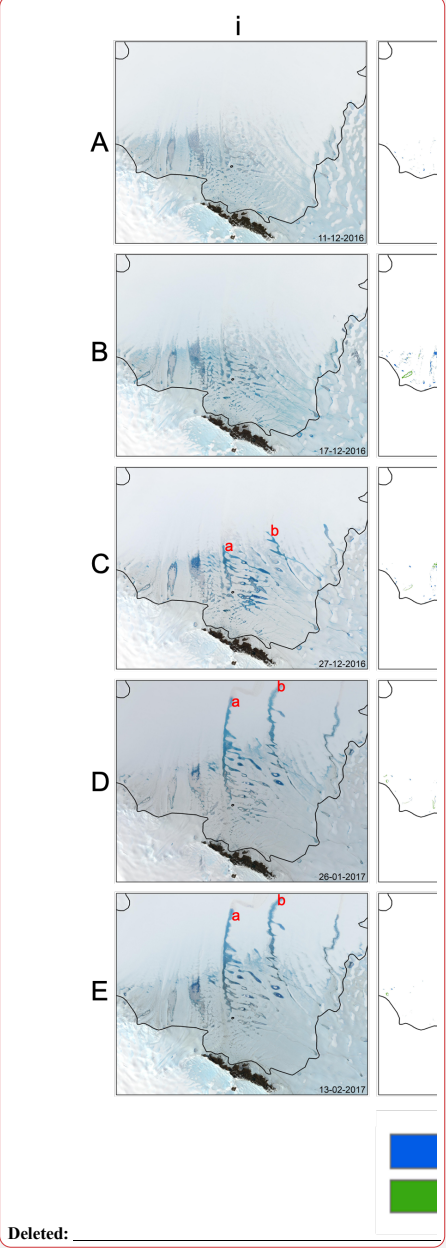
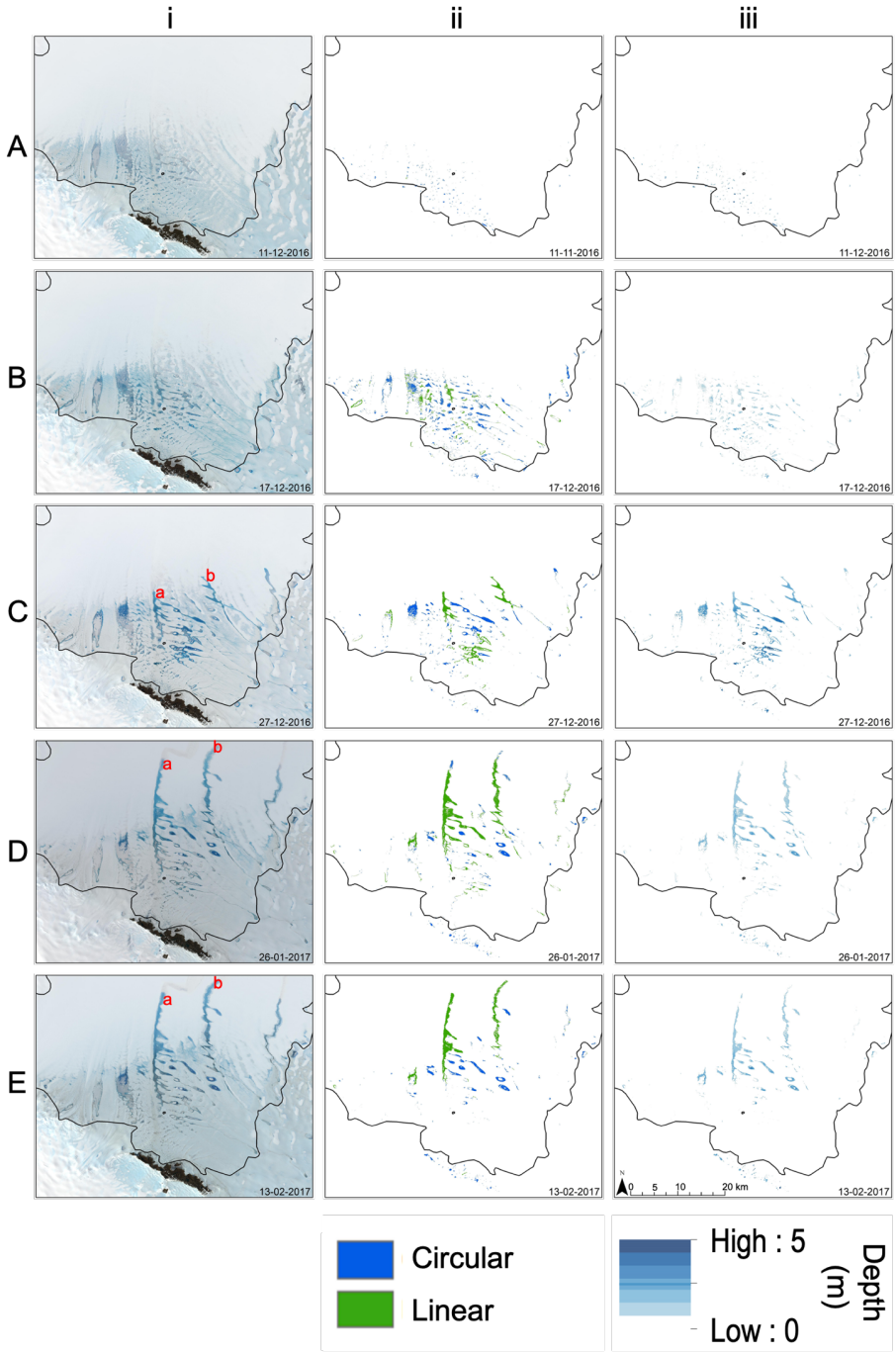
Figure 3: Solidity thresholds applied to water bodies identified on the Nivlisen Ice Shelf. The subset Sentinel-2 image is from the 26th January 2017, and the red box indicates the area shown in panels a-d. a) shows this area as an RGB, b) shows the water bodies identified and separated into linear or circular water bodies using a threshold of 0.42, c) a threshold of 0.45, and d) a threshold of 0.49.



1058
1059
1060
1061
1062
1063
1064

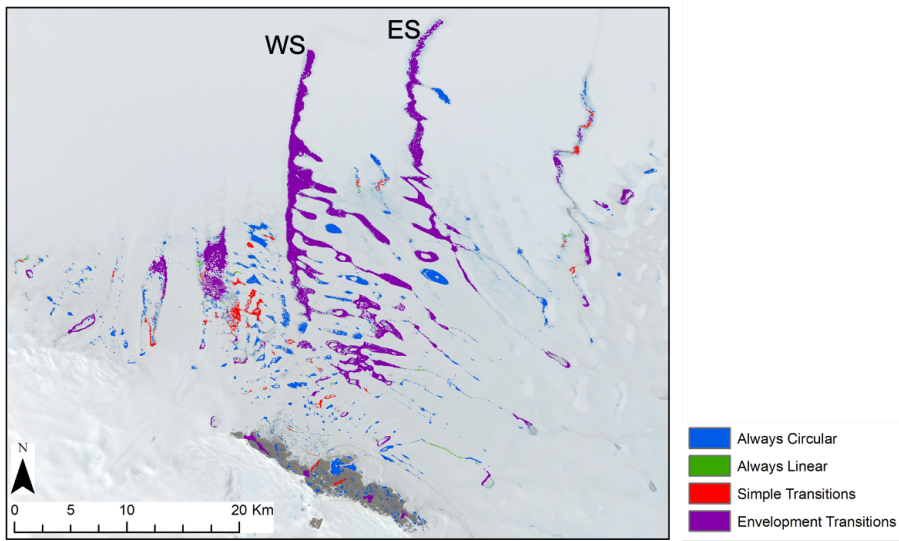
Figure 4: REMA DEM data for the Nivlisen Ice Shelf. a) the DEM; and b) overlain with the maximum melt extent matrix for the 2016-2017 melt season in white. DEM data sourced from the REMA dataset (Howat et al., 2019).

Formatted: Line spacing: Multiple 1.15 li



1067
1068 Figure 5: Five of the eleven dates studied in the 2016-2017 melt season (represented by labels A-
1069 E), and their corresponding (i) RGB images, (ii) area masks for circular and linear features, (iii) depth
1070 masks. Date stamps are in the bottom right hand corner of each image. Fig. S2 for all RGB images,
1071 Fig. S3 for all lake and stream area masks and Fig. S4 for all depth masks produced in this study.

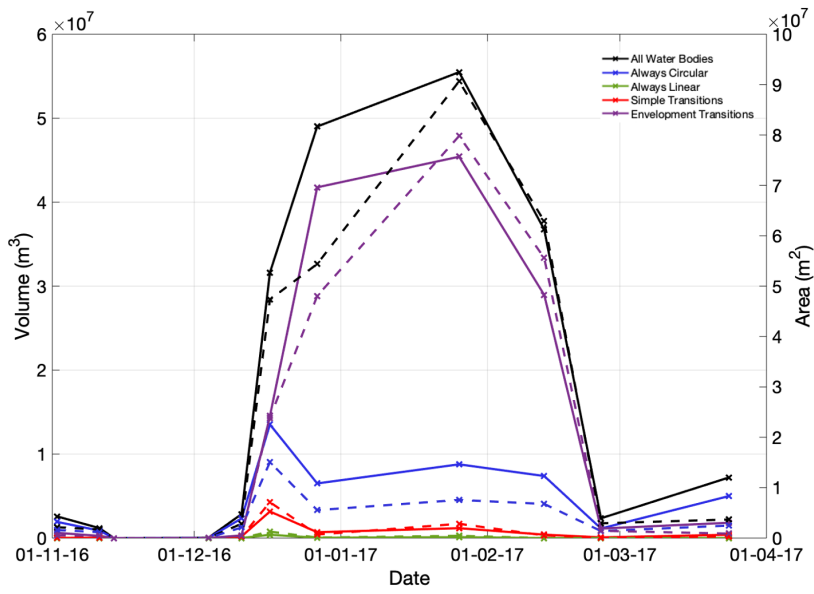
1072



1073
1074 Figure 6: Maximum extent of all identified water bodies on the Nivlisen Ice Shelf for the 2016-2017
1075 melt season, colour coded by water body type. 'WS' donates 'Western System', and 'ES' is
1076 Eastern System. Base image aquired by Sentinel-2 on 26th January 2017.

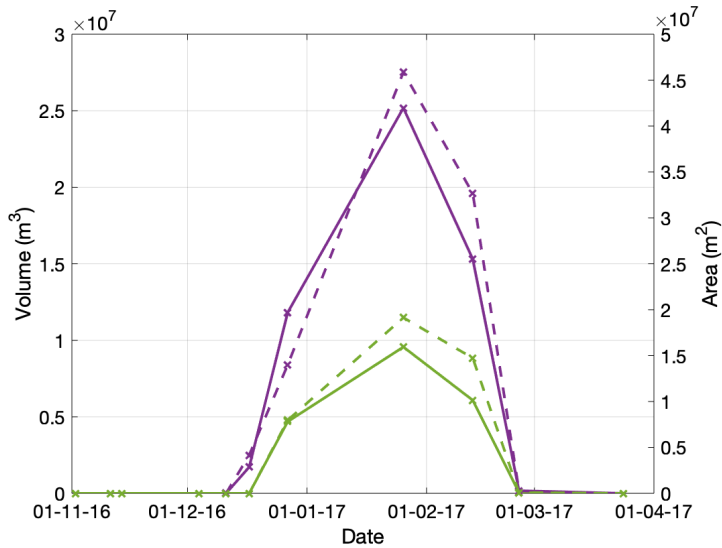
1077
1078
1079

Deleted: lake and stream

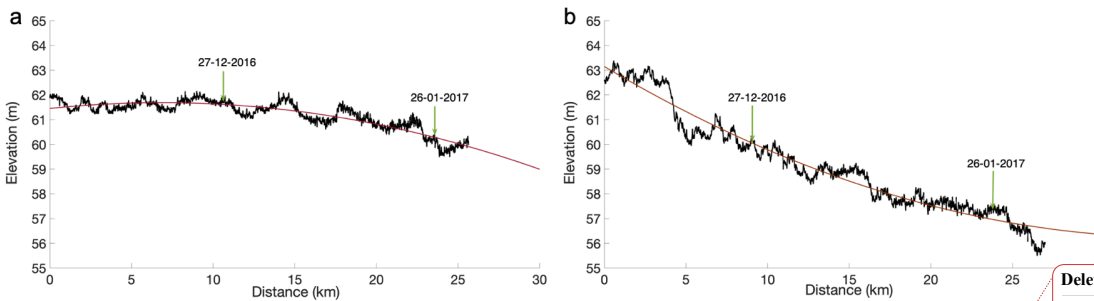


1081
 1082
 1083
 1084
 1085
 1086
 1087
 1088
 1089
 1090

Figure 7: Time series of the total area and volume held in each water body category over the 2016-2017 melt season on the Nivlisen Ice Shelf. Volumes are indicated by the solid lines, and areas by the dashed lines.



1091
 1092
 1093 Figure 8: Time series showing the area (dashed line) and volume (solid line) of the WS (purple)
 1094 and ES (green).
 1095

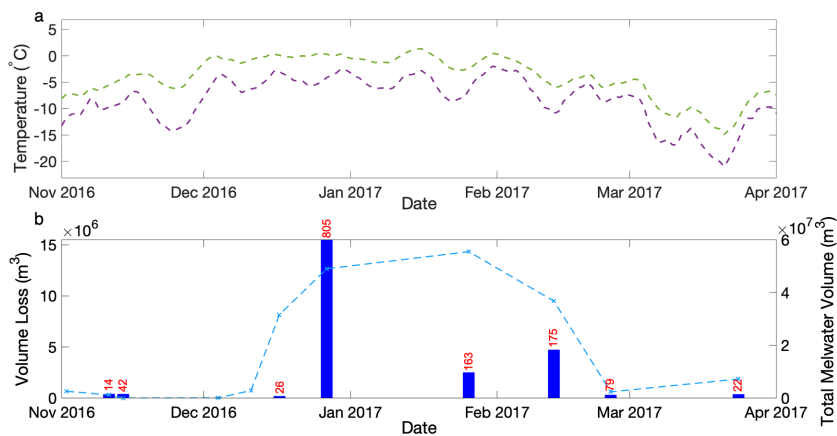


1096
 1097 Figure 9: Elevation profiles for (a) the WS and (b) the ES. Quadratic trendlines are shown
 1098 in red. Data are extracted from REMA (Howat et al., 2019) and the path of data extraction
 1099 was guided using the maximum depth matrix of both the WS and ES over the full 2016-
 1100 2017 melt season (see Fig. S5). The labelled green arrows mark the down-ice extent of
 1101 each system on the 27th December 2016 and 26th January 2017.

Deleted: ¶

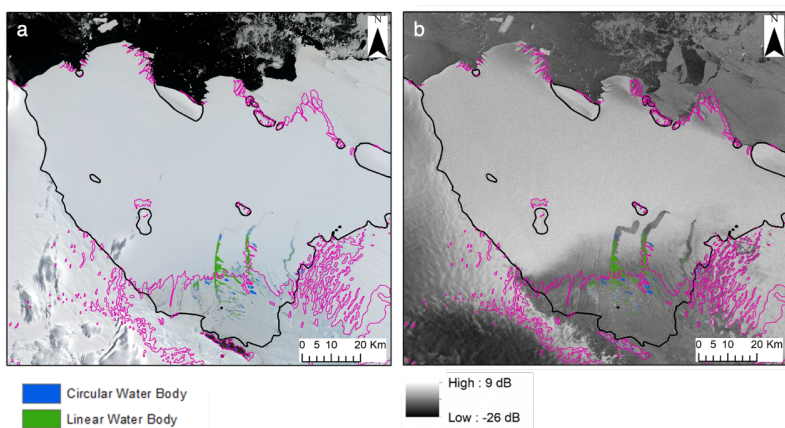
Formatted: Normal, Left, Level 1, Line spacing: Multiple 1.15 li

Formatted: Font: Helvetica



1104
1105
1106 Figure 10: Meteorological context of circular lake loss events: a) The seven day moving average
1107 of mean daily (purple line) and daily maximum (green line) near-surface air temperature from the
1108 MetUM simulation for the period from November 2016 to April 2017 at the model point immediately
1109 to the north of Schirmacheroasen. b) The total volume lost in 'loss events' by each image date
1110 from water bodies in the 'always circular' category (blue bars) and the total combined water volume
1111 (blue line). A loss event is defined as a > 80 % loss in water body volume through either lake
1112 drainage or freeze-through. The total number of loss events for each date is indicated above each
1113 bar.

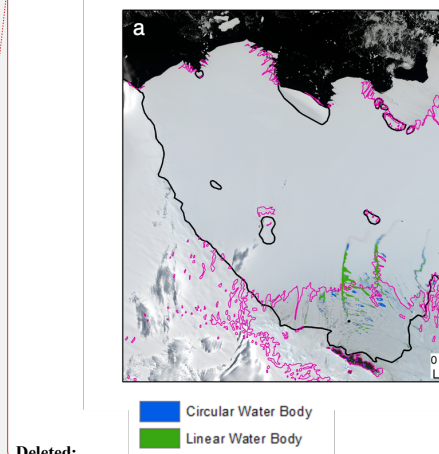
1114



1115
1116
1117 Figure 11: Comparison of optical imagery and radar imagery on 26th January 2017; a) is a
1118 mosaicked Sentinel-2 image, b) is a Sentinel-1 SAR image. Both a) and b) are overlain with the
1119 blue ice extent (pink) and the mapped area of all linear and circular surface water bodies, based on
1120 the FASTISH analysis of (a).

1121
1122

Deleted: south



Deleted:

1125
1126
1127
1128
1129

Table 1: Total area, total volume, and mean depth of all meltwater bodies on the Nivlisen Ice Shelf on various dates in the 2016-2017 melt season.

Date	Total Area (m ²)	Total Volume (m ³)	Mean Depth (m)	Max Depth (m)
2 nd November 2016	2.2 x 10 ⁶	2.6 x 10 ⁶	1.2	2.9
11 th November 2016	1.7 x 10 ⁶	1.2 x 10 ⁶	0.7	2.6
14 th November 2016	0.0	0.0	0.0	0.0
04 th December 2016	4.4 x 10 ⁴	4.0 x 10 ⁴	0.9	3.1
11 th December 2016	2.8 x 10 ⁶	2.8 x 10 ⁶	1.0	3.4
17 th December 2016	4.7 x 10 ⁷	3.2 x 10 ⁷	0.7	3.1
27 th December 2016	5.4 x 10 ⁷	4.9 x 10 ⁷	0.9	4.7
26 th January 2017	9.1 x 10 ⁷	5.5 x 10 ⁷	0.6	3.3
13 th February 2017	6.3 x 10 ⁷	3.7 x 10 ⁷	0.6	4.3
25 th February 2017	2.9 x 10 ⁶	2.4 x 10 ⁶	0.8	3.0
24 th March 2017	3.7 x 10 ⁶	7.2 x 10 ⁶	2.0	5.0

1130
1131
1132
1133
1134
1135
1136
1137
1138
1139
1140
1141
1142
1143
1144
1145
1146
1147

1148

1149 *Table 2: Maximum Area and Volume for each water body category on the Nivlisen Ice Shelf on*
1150 *various dates in the 2016-2017 melt season.*

1151

	Maximum Area (m ²)	Maximum Volume (m ³)	Date of Maximum Volume	Date of Maximum Area
All Water Bodies	9.1 x 10 ⁷	5.5 x 10 ⁷	26th January 2017	26th January 2017
Always Circular	1.5 x 10 ⁷	1.4 x 10 ⁷	17th December 2016	17th December 2016
Always Linear	1.3 x 10 ⁶	3.9 x 10 ⁵	17th December 2016	17th December 2016
Simple Transitions	3.2 x 10 ⁶	3.2 x 10 ⁶	17th December 2016	17th December 2016
Envelopment Transitions	8.0 x 10 ⁷	4.5 x 10 ⁷	26th January 2017	26th January 2017

Deleted: Lakes

Deleted: Streams

1152